



Imaging of Condensed Matter Magnetism Using an Atomic-Sized Sensor

Citation

Dovzhenko, Yuliya. 2018. Imaging of Condensed Matter Magnetism Using an Atomic-Sized Sensor. Doctoral dissertation, Harvard University, Graduate School of Arts & Sciences.

Permanent link

<http://nrs.harvard.edu/urn-3:HUL.InstRepos:41129200>

Terms of Use

This article was downloaded from Harvard University's DASH repository, and is made available under the terms and conditions applicable to Other Posted Material, as set forth at <http://nrs.harvard.edu/urn-3:HUL.InstRepos:dash.current.terms-of-use#LAA>

Share Your Story

The Harvard community has made this article openly available.
Please share how this access benefits you. [Submit a story](#).

[Accessibility](#)

Imaging of Condensed Matter Magnetism Using an Atomic-Sized Sensor

A dissertation presented
by

Yuliya Dovzhenko

to

The Department of Physics
in partial fulfillment of the requirements
for the degree of
Doctor of Philosophy
in the subject of

Physics

Harvard University
Cambridge, Massachusetts

April 2018

©2018 - Yuliya Dovzhenko

All rights reserved.

Dissertation advisor

Author

Professor Amir Yacoby

Yuliya Dovzhenko

Imaging of Condensed Matter Magnetism Using an Atomic-Sized Sensor

Abstract

The development of increasingly sensitive scanning techniques has enabled valuable insights into the physics of interacting condensed matter systems. Recently a new kind of local probe based on Nitrogen-Vacancy (NV) centers in diamond has emerged as a powerful magnetic imaging platform. The NV center has been used for a variety of local measurements including measurements of magnetic fields[1], imaging of single electron spins with nanometer resolution[2], magnetic resonance detection of single nuclear spins[3], as well as measurements of temperature[4] and electric fields[5]. However, imaging an a priori unknown static magnetization structure using a NV center magnetometer is inherently difficult because infinitely many magnetization patterns can produce identical local magnetic fields. In this work I use a scanning NV center magnetometer to image topologically non-trivial magnetization patterns in stacks of thin magnetic films, in which skyrmions had been predicted[10]. I will summarize the details of the experiment crucial to obtaining these data as well as our method for extracting the underlying magnetization structure. As a result of this experiment, we discover a never-before observed type of skyrmion tube whose structure rotates from top to bottom, which has since been confirmed by another technique[11].

Contents

Title Page	i
Abstract	iii
Table of Contents	iv
Citations to Previously Published Work	vi
Acknowledgments	vii
Dedication	viii
1 Introduction	1
1.1 Introduction to Nitrogen-Vacancy center magnetometry	2
1.2 Structure of the thesis	5
2 Nitrogen-Vacancy center as a magnetometer	6
2.1 Electronic structure of the NV center	8
2.2 NV center in an external magnetic field	10
2.2.1 Effect of magnetic fields on NV photoluminescence	13
2.2.2 Quantitative sensing of magnetic fields	14
2.2.3 Reconstruction of the field components	14
2.3 NV magnetometry of a static magnetization structure	17
2.4 Summary	20
3 Experimental Setup	21
3.1 Overview of the experiment	21
3.2 Room-temperature experiment	23
3.2.1 Scanning NV tip	23
3.2.2 Scanning sample tip	24
3.2.3 Performing a magnetometry scan	26
3.2.4 Troubleshooting commonly encountered problems	28
3.3 Low-temperature experiment and early results	31
4 Magnetic skyrmions	35
4.1 Introduction to magnetic skyrmions	35

4.2	Thin-film skyrmions at room temperature	37
4.3	Magnetic structure in a single Pt/CoFeB stack	40
4.3.1	Continuous film	42
4.3.2	Patterned film	43
4.4	Skyrmion in a multistack film	47
5	Solving for the skyrmion magnetization structure	52
5.1	Gauge-dependent solutions for the magnetization pattern	53
5.1.1	Bloch gauge	54
5.1.2	Néel gauge	56
5.1.3	Intermediate gauge	57
5.2	Twisted structure	59
6	Conclusions and Outlook	63
A	Calibration of the film thickness and saturation magnetization	66
	Bibliography	70

Citations to Previously Published Work

Large portions of Chapters 4 and 5 have appeared in the following paper:

Y. Dovzhenko, F. Casola, S. Schlotter, T. X. Zhou, F. Büttner, R. L. Walsworth, G. S. D. Beach, and A. Yacoby, “Imaging the spin texture of a skyrmion under ambient conditions using an atomic-sized sensor”, *Nature Communications* (in press 2018).

Acknowledgments

I was incredibly lucky to be able to pursue a PhD in Prof. Yacoby's lab at Harvard. I had access to incredible colleagues, plenty of opportunities for learning and exploration, and endless experimental capabilities of the Physics department and the School of Engineering. Prof. Yacoby has provided the perfect balance between guidance and freedom. It was an honor to have Prof. Sachdev and Prof. Walsworth on my committee to provide insights into my research. Prof. Walsworth was also particularly helpful in life and career advice.

A large fraction of the work in this thesis was done in close collaboration with Dr. Francesco Casola, and would not be possible without his help. I have learned from his creativity in solving problems and his resolve to keep going despite the very experimental nature of our work.

I was honored to collaborate with Prof. Geoff Beach, Sarah Schlotter and Dr. Felix Büttner, who were instrumental in shaping our measurements and understanding our conclusions. In particular, I am grateful to Sarah for bringing her expertise and hard work to developing the magnetic films I measured. Another essential contributor to the development of our diamonds and scanning tips is Tony Zhou, who found ingenious approaches to sample fabrication.

Finally, I owe a debt of gratitude to my wonderful officemates Shannon Harvey and Andrei Levin for many years of support, mentorship and entertainment.

To my family.

Chapter 1

Introduction

Scanning experiments have played an essential role in the advancement of condensed matter over the last few decades. Among the most notable success stories is spin-resolved scanning tunneling microscopy, which has enabled physicists to detect single electron spins[12] and assemble magnetic atoms into arbitrary structures to probe and manipulate their interactions[13]. A scanning single-electron transistor has been used to image localized quasiparticle states, which do not contribute to the electronic transport in the fractional quantum Hall regime[14]. Scanning magnetometry techniques have been successfully used to supplement transport measurements with additional spatial information. For example, a scanning superconducting quantum interference device was used to image two-dimensional current patterns in HgTe quantum wells and unambiguously differentiate between bulk conduction and edge conduction in the quantum spin Hall state[15]. A scanning Nitrogen-Vacancy (NV) center has been used to image current flow patterns in graphene[16].

While reconstructing two-dimensional current patterns from maps of magnetic

fields is a well-established technique[17], reconstructing magnetization patterns from their magnetic fields is significantly more difficult because in general infinitely many solutions exist[18]. In this thesis we aim to demonstrate, despite these limitations, the promise of scanning NV magnetometry when applied to the study of nanoscale magnetization structures in condensed matter.

1.1 Introduction to Nitrogen-Vacancy center magnetometry

The NV center is a substitutional defect in a diamond lattice possessing an effective $S = 1$ spin degree of freedom, which can be initialized, controlled and read out optically. Because it retains its spin coherence properties across a wide range of temperatures and can be integrated into a robust diamond nanostructure, this color center has emerged as a promising platform for nanoscale magnetic sensing[19, 20]. Some of the unique advantages of the NV center are listed below:

- **Atomic-sized sensor of magnetic fields.** Because of the spatial confinement of its local spin density to a volume below 1 nm^3 (see Ref. [21]), a NV center in diamond is effectively a point-like sensor of magnetic fields. This is in contrast to techniques such as nano-SQUID, another promising local magnetometry technique, which is capable of measuring magnetic flux through a 75 nm diameter area[22]. The NV center's spatial resolution is usually limited by its distance to the sample being measured.

- **Optical initialization and readout.** The NV center's $S = 1$ spin degree of freedom can be read out optically by measuring the NV photoluminescence, as will be explained in Chapter 2. Furthermore, under continuous optical excitation the NV spin state will decay to the $m_s = 0$ spin state, thus enabling spin state initialization[23].
- **Coherence in a wide range of temperatures and magnetic fields**[6, 7, 8, 9]. In this work I will report magnetometry results at room temperature as well as a new experimental setup for scanning magnetometry at cryogenic temperatures.
- **Broad frequency range.** The NV center can be used to measure both DC and AC magnetic fields with frequencies as high as 115 GHz[9]. The NV center also offers in principle arbitrary frequency resolution when a lock-in measurement is carried out synchronously over multiple re-initializations of the NV spin state[24, 25].
- **Non-invasive sensing.** The NV center's magnetic moment is very weak compared to a typical magnetic tip used in magnetic resonance force microscopy[26], another promising technique capable of detecting a single electron spin. Furthermore, due to diamond's chemical inertness the NV center can be put in close contact with many different samples including living cells and organisms[4, 27].

A scanning NV center has been used to perform nanoscale measurements of temperature[4], electric fields[5], as well as oscillating magnetic fields from precessing spins in nuclear magnetic resonance (NMR) and magnetic resonance imaging (MRI)-type ex-

periments. Notable examples include imaging a single electron spin with 1 nm resolution[2], detecting a single nuclear spin[28] and an ensemble of nuclear spins in a very small (1 picoliter) sample with unprecedented frequency resolution of about 3 Hz[24, 25]. An overview of the NV center’s achievements in condensed matter magnetometry to date can be found in Ref. [29]. In this work I will focus on the scanning NV center as a probe of DC magnetic fields produced by static magnetization patterns in condensed matter systems.

In the last few years NV magnetometry has started to emerge as a scanning probe for condensed matter phenomena. Examples of systems studied by scanning NVs include two-dimensional current patterns in graphene[16], domain walls in a ferromagnetic material[30] and vortices in superconductors[6]. When applied to static magnetization distributions, the technique has fundamental limitations, which I will discuss in Chapter 2, because the NV center measures magnetic fields produced by the sample magnetization rather than probing the magnetization directly. The majority of NV studies of magnetic structures to date have started with a proposed model and then fit the measured magnetometry data to it[30, 31]. In this work we attempt to go in the opposite direction, starting with the scan data and very few assumptions (e.g. that there is no magnetization outside of the magnetic material) and work to extract as much information as possible about the underlying magnetization pattern (see discussion in Chapter 5). We discover a new type of twisted skyrmion structure present in magnetic thin film multilayer stacks at room temperature, which has since been confirmed by another independent experiment using circular dichroism in X-ray magnetic scattering [11].

1.2 Structure of the thesis

This thesis has the following structure: I will introduce and briefly motivate the properties of the NV center, which enable us to perform scanning magnetometry, in Chapter 2. The details of integrating of the NV center into a scanning setup and performing measurements on a magnetic sample will be covered in Chapter 3. Since previous dissertations[32, 33] from our group have already introduced the room-temperature scanning NV setup and diamond fabrication procedures, I will focus in particular on new aspects of the experiment which I developed in order to image magnetic films. In Chapter 4 I will summarize the data taken in the effort to image a room-temperature thin-film skyrmion. Finally, Chapter 5 will explain how to narrow down the number of possible magnetization structures compatible with the data and use a single magnetometry scan to not only solve for three components of sample magnetization, but also infer information about the depth dependence of the magnetization structure.

Chapter 2

Nitrogen-Vacancy center as a magnetometer

The NV center has a few key properties which make it an attractive candidate for scanning magnetometry, which are summarized in Fig. 2.1. The center consists of a substitutional Nitrogen atom in a diamond lattice located next to a Carbon vacancy (see sketch in Fig. 2.1a). In this work I will only discuss the NV^- , the negatively charged NV center, as opposed to the neutral NV^0 defect[34]. The electronic ground state of the NV^- center possesses a $S = 1$ electronic spin. The center's promise as a magnetometer lies in the possibility to optically initialize and read out its electronic spin state, which will be explained later in this chapter. As indicated schematically in Fig. 2.1b, the NV spin states differ in the number of photons emitted under optical excitation: the state with $|m_s = 0\rangle$ is brighter than states with $|m_s = \pm 1\rangle$. We can measure the energy splittings between different spin states by performing an Electron Spin Resonance (ESR) experiment[35]. We will record the NV photolumines-

cence (PL) under continuous optical excitation while applying an external oscillating magnetic field of variable frequency. When the drive frequency matches an energy splitting between $|m_s = 0\rangle$ and one of the states with $|m_s = \pm 1\rangle$, the spin state will undergo oscillations between these states leading to a reduction in NV PL on average. An example of such a measurement indicating a spin transition near 2.45 GHz is plotted in Fig. 2.1c. Finally, in order to turn the NV center into a scanning sensor we can fabricate a scanning probe around a single NV center thanks to diamond's mechanical robustness and compatibility with nanofabrication techniques[36, 37].

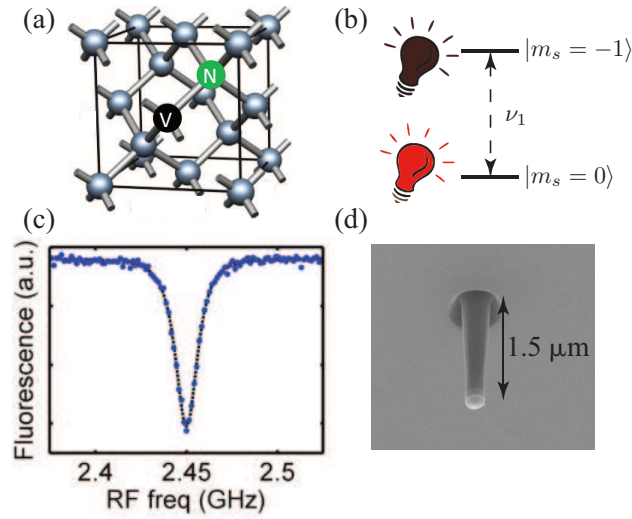


Figure 2.1: Summary of the NV center properties relevant to scanning magnetometry. Panel (a) shows a sketch of the NV center in the diamond lattice. Depending on the electronic spin state of the center, it will emit a different number of photons under continuous excitation, as indicated in sketch (b). To measure the energy difference between different spin levels, we can collect NV fluorescence while applying an external radio-frequency (RF) magnetic field of varying frequency. When the applied frequency matches the energy splitting, we observe a change in fluorescence. An example of such a measurement is shown in plot (c). The diamond crystal surrounding the NV center can be etched to form a scanning tip, as seen in a scanning electron microscopy image (d).

2.1 Electronic structure of the NV center

We can gain an intuition for the NV electronic structure by considering its spatial symmetries (see for example Ref. [38] for a full derivation or Ref. [39] for a brief summary). It is widely believed that the NV electronic structure is formed by four dangling bonds: one from the substitutional Nitrogen atom and three from surrounding Carbon atoms (see Fig. 2.2)[39]. We will denote these orbitals by n, c_1, c_2 , and c_3 correspondingly. The center belongs in the C_{3v} crystallographic symmetry group (three-fold rotation symmetry about a vertical axis). This group has three irreducible representations (IR's): two rank-one IR's and one rank-two IR. Applying projection operators to the dangling bonds n, c_1, c_2, c_3 yields four molecular orbitals which transform like the IR's of the group.

The NV center is believed to contain six bound electrons, which is two electrons short of the eight electrons needed to fill all available orbital and spin states. Thus the problem can be restated in terms of two holes instead of six electrons. The eigenstates and degeneracies can be obtained from the irreducible representations of the direct product $C_{3v} \times C_{3v}$. Finally, complete two-hole eigenstates can be constructed by enforcing that the full wavefunction be anti-symmetric. The resulting states can be found in Refs. [38, 40]. A schematic of the state structure, focusing only on the states relevant to this work, is shown in Fig. 2.3.

The ground state is a spin triplet with $|m_s = 0\rangle$ state split from $|m_s = \pm 1\rangle$ states by D , the zero-field splitting. The $|m_s = \pm 1\rangle$ states can be further Zeeman-split in presence of an external magnetic field. An optical transition between the ground state and the lowest excited state triplet has a wavelength of 637 nm, but can be excited by

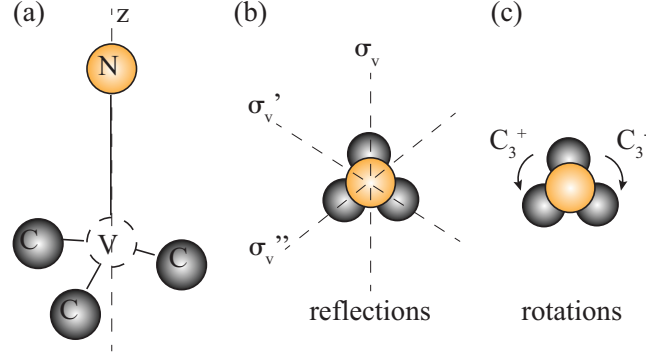


Figure 2.2: A schematic representation of the symmetries of the NV center. In sketch (a) spheres represent Nitrogen and Carbon atoms, and lines represent dangling bonds. The symmetry group of the NV center contains the following operations: three reflections about vertical planes and two rotations by $2\pi/3$. The reflection planes are indicated by dashed lines in (b), and are labeled by σ_v, σ'_v and σ''_v . The rotations are labeled by C_3^\pm in panel (c).

a broad range of optical frequencies due to phonon broadening of the NV states[39].

In this work we excite the NV optical transition with a 532 nm laser, which allows us to separate the excitation photons from the emitted photons by their color.

The optical initialization and readout mechanism relies on one crucial property: states with $|m_s = 0\rangle$ will cycle between ground and excited orbital states under optical excitation, while states with $|m_s = \pm 1\rangle$ have a small probability of crossing into the singlet states via spin-orbit interaction and subsequently decaying into $|m_s = 0\rangle$. Because transitions into and out of the single states are non-radiative, states with $|m_s = \pm 1\rangle$ will emit fewer photons and eventually decay into $|m_s = 0\rangle$

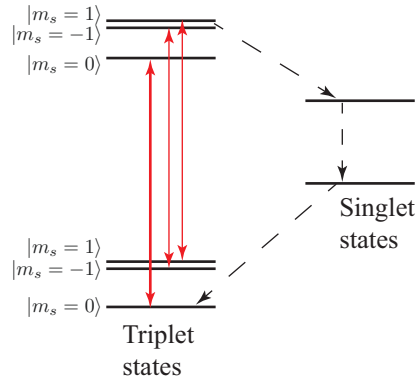


Figure 2.3: The NV level structure. For simplicity, only the states relevant to our work are shown. The transitions between the ground and excited triplet states are spin-conserving. Solid red arrows indicate transitions which involve an absorption or emission of a photon, while transitions indicated by dashed lines are non-radiative.

under continuous optical excitation, thus providing both an initialization and readout mechanism[41].

2.2 NV center in an external magnetic field

To solve for the NV center spin state in external magnetic field, we need to take into account the following: Zeeman splitting between the $|m_s = \pm 1\rangle$ states and the zero-field splitting which lifts both $|m_s = \pm 1\rangle$ states in energy above the $|m_s = 0\rangle$ state. For the purpose of this work, the NV center can be effectively modeled by the following Hamiltonian[8]:

$$\mathcal{H} = \gamma (B_x S_x + B_y S_y + B_z S_z) + D S_z^2, \quad (2.1)$$

where $\gamma = 2.8025$ MHz/G is the gyromagnetic ratio of the NV center spin measured experimentally on one of the NV centers used in this work, D represents the zero-

field splitting between $|m_s = 0\rangle$ and $|m_s = \pm 1\rangle$ states, and we have assumed for simplicity that the NV center's quantization axis points along the z -direction. Thus, B_z is the component of the external magnetic field along the NV axis, while (B_x, B_y) are perpendicular to it. (S_x, S_y, S_z) are the spin-1 Pauli spin matrices. In order to stay consistent with the notation in the rest of our work, we rewrite B_z as B_{\parallel} , and $(B_x S_x + B_y S_y)$ as $B_{\perp} \cdot S_{\perp}$:

$$\mathcal{H} = D(\hat{S}_{\parallel})^2 + \gamma B_{\parallel} \hat{S}_{\parallel} + \gamma B_{\perp} \cdot \hat{S}_{\perp}. \quad (2.2)$$

To measure the external magnetic field along the NV axis, we examine the energy

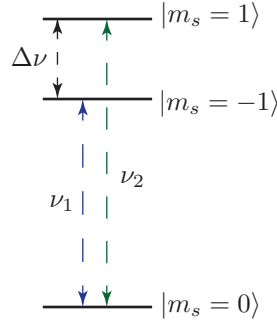


Figure 2.4: An illustration of the notation we use to describe energy splittings between the $|m_s = 0\rangle$ level and the $|m_s = \pm 1\rangle$ levels.

splittings between the NV spin states $|m_s = 0\rangle$ and $|m_s = \pm 1\rangle$. Our notation for two frequencies associated with these spin transitions is shown schematically in Fig. 2.4. In the presence of magnetic fields perpendicular to the NV axis, NV spin states will get mixed. However, at small perpendicular fields we will continue to refer to ν_1 as the transition frequency between the mostly $|m_s = 0\rangle$ and the mostly $|m_s = -1\rangle$ state, and ν_2 between mostly $|m_s = 0\rangle$ and $|m_s = 1\rangle$.

Diagonalizing Eq. 2.1 leads to energy splittings plotted in Fig. 2.5. In the case of a field parallel to the NV axis, we observe a linear shift in ν_1 and ν_2 in opposite directions. If an external B_\perp is applied while B_\parallel is kept constant, both ν_1, ν_2 increase. The values of ν_1, ν_2 can be used to extract the magnitude of B_\perp , the external perpendicular field, but not its direction. Furthermore, the effect of B_\perp on $\nu_{1,2}$ is second-order at small values of B_\perp , leading to a much lower sensitivity compared to the measurement of B_\parallel , given the same amount of uncertainty in the measurement of $\nu_{1,2}$.

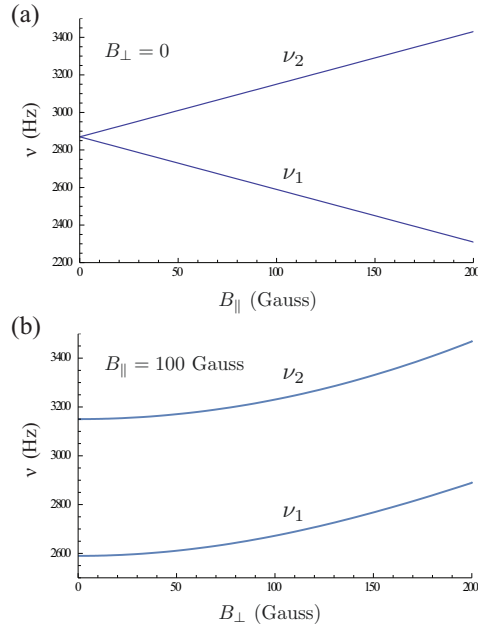


Figure 2.5: Frequencies associated with NV center spin transitions in presence of variable external magnetic fields. (a): ν_1, ν_2 as function of externally applied B_\parallel in the absence of any B_\perp . (b): ν_1, ν_2 as function of B_\perp , which is applied in addition to a fixed $B_\parallel = 100$ Gauss.

2.2.1 Effect of magnetic fields on NV photoluminescence

When B_{\perp} in the excess of a few tens of Gauss is applied, the NV spin states become mixed, leading to a reduction in NV PL. This process can be modeled using a straightforward state transition rate model found in Ref. [42]. The fraction of remaining NV PL as function of applied B_{\parallel} and B_{\perp} is plotted in Fig. 2.6. In addition to the PL alone, the contrast of an ESR measurement is also reduced because of the mixing of the levels. This leads to a significant limitation of NV magnetometry: it is very difficult to measure samples producing over 150 Gauss of field perpendicular to the NV axis.

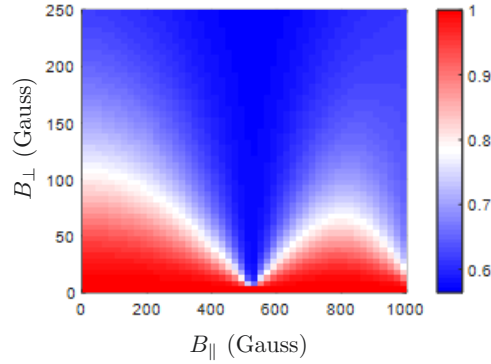


Figure 2.6: Simulated NV center fluorescence as function of magnetic fields parallel and perpendicular to the NV center axis.

In the intermediate regime of over a few tens of Gauss, this PL reduction can be used as a fast qualitative imaging mode. By recording PL while scanning over a sample we can get an indication of the domains in the sample. This imaging mode is similar to magnetic force microscopy[43] but can offer higher spatial resolution, and has negligible effect on the magnetization in the sample. For example, Fig. 2.7 shows a PL map of a micron-sized magnetic dot hosting a few striped domains. While this

image does not provide quantitative information about the magnetic structure in the sample, it does reveal approximately periodic parallel domains.

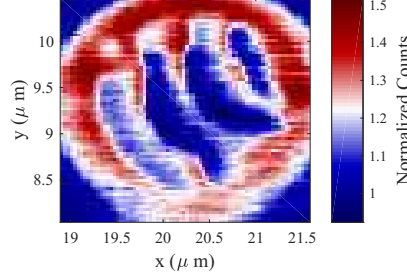


Figure 2.7: A map of NV PL while scanning over a thin magnetic disc reveals a multidomain state.

2.2.2 Quantitative sensing of magnetic fields

The NV center allows us to precisely measure magnetic fields parallel to its quantization axis. In this work we use [100]-cut diamond substrates. Out of four possible orientations, we choose NV centers whose axis lies in the zx -plane tilted from the z -axis by an angle $\theta_{\text{NV}} = \arccos(1/\sqrt{3})$. A typical magnetometry scan will record the upper (ν_2) and lower (ν_1) NV resonance frequencies at each point in space. We can solve for B_{\parallel} and B_{\perp} from measured ν_1, ν_2 using the following equations[44]:

$$B_{\parallel} = \frac{\sqrt{-(D + \nu_2 - 2\nu_1)(D + \nu_1 - 2\nu_2)(D + \nu_1 + \nu_2)}}{3\gamma\sqrt{3D}}, \quad (2.3)$$

$$B_{\perp} = \frac{\sqrt{-(2D - \nu_2 - \nu_1)(2D + 2\nu_1 - \nu_2)(2D - \nu_1 + 2\nu_2)}}{3\gamma\sqrt{3D}}. \quad (2.4)$$

2.2.3 Reconstruction of the field components

We measure the stray field $B_{\parallel}(\mathbf{p}, d)$ in a plane at a distance d from the magnetic surface, where \mathbf{p} is a two-dimensional vector describing the position of the NV in

the xy - plane (see Fig. 2.8 for an illustration of our coordinate system). At the probe position the stray field is curl-free, and thus can be expressed in terms of a magnetostatic potential ϕ_M [45, 46]:

$$\mathbf{B} = -\nabla\phi_M(\boldsymbol{\rho}), \quad (2.5)$$

where the three components of the \mathbf{B} vector are spatial derivatives of a scalar function. This is a hint that different components of the magnetic field are in general not independent[18, 45]. Our measurement scheme provides further opportunities for simplifying assumptions since the only sources of magnetic field are located in a 2D plane parallel to the scanning plane of the NV. We find it useful to take a 2D Fourier transform of the measured magnetic field $\mathbf{B}(\boldsymbol{\rho}, d)$ [44]:

$$\mathbf{B}(\mathbf{k}, d) = \int_0^{2\pi} \int_0^\infty \mathbf{B}(\boldsymbol{\rho}, d) e^{-ik\rho \cos(\phi - \phi_k)} \rho d\rho d\phi. \quad (2.6)$$

The vectors $\boldsymbol{\rho}$ and \mathbf{k} are 2-dimensional vectors in real and reciprocal space re-

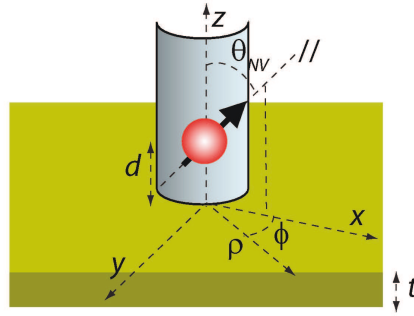


Figure 2.8: An illustration of the coordinate system used in this work. The sketch depicts an NV center in a $[100]$ -cut diamond pillar. The NV quantization axis lies in the zx -plane tilted from the vertical by $\theta_{NV} = 54.7^\circ$. The NV has a distance d from the surface of the magnetic material of thickness t .

spectively, forming angles ϕ_k and ϕ with the x -direction (see a schematic drawing

in Fig. 2.8). As derived in Ref.[44], when the stray field is produced by a sheet of magnetic dipoles distributed over a thickness t and with local magnetization $M_s \mathbf{m}(\mathbf{\rho}_j) = M_s[m_x(\mathbf{\rho}_j), m_y(\mathbf{\rho}_j), m_z(\mathbf{\rho}_j)]$, the stray field can be written in momentum space as:

$$\mathbf{B}(\mathbf{k}, d) = \mathbf{D}(\mathbf{k}, d) \mathbf{m}(\mathbf{k}), \quad (2.7)$$

where $\mathcal{D}(\mathbf{k}, d)$ is a traceless symmetric kernel matrix:

$$\mathbf{D}(\mathbf{k}, d) = \frac{\mu_0 M_s}{2} (e^{-dk} - e^{-(d+t)k}) \begin{pmatrix} -\cos^2(\phi_k) & -\frac{\sin(2\phi_k)}{2} & -i \cos(\phi_k) \\ -\frac{\sin(2\phi_k)}{2} & -\sin^2(\phi_k) & -i \sin(\phi_k) \\ -i \cos(\phi_k) & -i \sin(\phi_k) & 1 \end{pmatrix}. \quad (2.8)$$

We account for the finite size film thickness t by assuming the local magnetization vector $\mathbf{m}(\mathbf{\rho}_j)$ to be constant through the magnetic film thickness and therefore integrating that dimension out. M_s is the nominal, space-independent, saturation magnetization of the magnetic film. The validity of this assumption will be addressed further in Chapter 5.

From Eq. (2.8) we can immediately realize that the rows of the matrix $\mathbf{D}(\mathbf{k}, d)$ are multiples of each other, and therefore the matrix is not invertible. This means that, given all three components of \mathbf{B} , we cannot solve for \mathbf{m} . It also means that we may be able to obtain all three components of \mathbf{B} from a measurement of the field along just one axis (in our case, NV axis).

Given a 2D Fourier transform of a magnetometry scan, $B_{\parallel}(\mathbf{k}, d)$, we can solve for the stray field component along the z -axis $B_z(\mathbf{k}, d)$ (see Fig. 2.8):

$$B_z(\mathbf{k}, d) = \frac{B_{\parallel}(\mathbf{k}, d)}{\cos(\theta_{NV}) - i \sin(\theta_{NV}) \cos(\phi_k)}, \quad (2.9)$$

and then perform an inverse Fourier transform to obtain a real space map of $B_z(\boldsymbol{\rho}, d)$. Any other component of \mathbf{B} can be reconstructed without singularities from a single measurement of $B_{\parallel}(\boldsymbol{\rho}, d)$ within a whole plane, provided $\theta_{NV} \neq \pi/2$.

It is important to note that the proportionality between different components of the field only holds in Fourier space. The reconstruction procedure will only be accurate for the k -components of the field that are present in the scan. It cannot be applied to a single point measurement. It also drops the $k = 0$ component of the field. Ideally, the scan should include the sample boundaries in order for the reconstruction to be rigorously correct. Reconstruction of incomplete scans could in principle be possible if there are symmetries in the system by setting appropriate boundary conditions. We leave these extensions to future work in the NV community.

Finally, there is an analogy with the Huygens principle in optics. Given a map of the magnetic field at a distance d from the field, we can calculate the map at a different distance $d' = d + h$ by multiplying the Fourier transform of the map at d by the prefactor $\exp(-kh)$. This means that little additional information can be gained by taking multiple scans at different offsets from the surface. Procedures for upward or downward propagation for $h > 0$ or $h < 0$ have been discussed in the literature[45].

2.3 NV magnetometry of a static magnetization structure

We have seen that the Fourier-space expression for magnetic field $\mathbf{B}(\mathbf{k})$ in Eqs. 2.7-2.8 provides an intuitive explanation for the interdependence of the field components.

In order to understand the dependence of \mathbf{B} on the underlying magnetization pattern $\mathbf{m}(\boldsymbol{\rho})$ we examine the real-space expression for the magnetic field, derived in Ref. [47].

Starting from Eq. 2.7, we can express all functions of angle ϕ_k in terms of k_x, k_y, k . When transforming from inverse space to real space, the factors of k_x, k_y become derivatives, and products become convolutions. The resulting expression for $\mathbf{B}(\boldsymbol{\rho}, d)$ is:

$$\mathbf{B}(\boldsymbol{\rho}, d) = -\frac{\mu_0 M_s}{2} \begin{pmatrix} -\alpha_z(d, t) * \frac{\partial^2}{\partial x^2} & -\alpha_z(d, t) * \frac{\partial^2}{\partial y \partial x} & \alpha_{x,y}(d, t) * \frac{\partial}{\partial x} \\ -\alpha_z(d, t) * \frac{\partial^2}{\partial y \partial x} & -\alpha_z(d, t) * \frac{\partial^2}{\partial y^2} & \alpha_{x,y}(d, t) * \frac{\partial}{\partial y} \\ \alpha_{x,y}(d, t) * \frac{\partial}{\partial x} & \alpha_{x,y}(d, t) * \frac{\partial}{\partial y} & \alpha_z(d, t) * \nabla^2 \end{pmatrix} \begin{pmatrix} m_x(\boldsymbol{\rho}) \\ m_y(\boldsymbol{\rho}) \\ m_z(\boldsymbol{\rho}) \end{pmatrix}, \quad (2.10)$$

where we have defined *resolution function* $\alpha_{x,y}(d, t)$ of the in-plane magnetization as:

$$\begin{aligned} \alpha_{x,y}(d, t) &= \frac{1}{(2\pi)^2} \int_{\mathbf{k}} \frac{e^{-(d+t)k} (e^{tk} - 1)}{k} e^{i\mathbf{k} \cdot \boldsymbol{\rho}} d\mathbf{k} \\ &= \frac{1}{2\pi} \left(\frac{1}{\sqrt{d^2 + r^2}} - \frac{1}{\sqrt{(d+t)^2 + r^2}} \right). \end{aligned} \quad (2.11)$$

Note that if $t \ll d$ the previous resolution function can be simplified as:

$$\alpha_{x,y}(d, t \ll d) \approx \frac{1}{2\pi} \frac{dt}{(d^2 + r^2)^{3/2}}. \quad (2.12)$$

Similarly, the resolution function $\alpha_z(d, t)$ of the out-of-plane magnetization is:

$$\begin{aligned} \alpha_z(d, t) &= \frac{1}{(2\pi)^2} \int_{\mathbf{k}} \frac{e^{-(d+t)k} (e^{tk} - 1)}{k^2} e^{i\mathbf{k} \cdot \boldsymbol{\rho}} d\mathbf{k} \\ &= -\frac{1}{(2\pi)^2} \int_{d'} \int_{\mathbf{k}} \frac{e^{-(d'+t)k} (e^{tk} - 1)}{k} e^{i\mathbf{k} \cdot \boldsymbol{\rho}} d\mathbf{k} dd' \\ &= -\int \alpha_{x,y}(d', t) dd' = \frac{1}{2\pi} \log \left(\frac{d + t + \sqrt{(d+t)^2 + r^2}}{d + \sqrt{d^2 + r^2}} \right). \end{aligned} \quad (2.13)$$

In the limit $t \ll d$ the previous resolution function can be simplified as:

$$\alpha_z(d, t \ll d) \approx \frac{1}{2\pi} \frac{t}{(d^2 + r^2)^{1/2}}. \quad (2.14)$$

A single component of the stray magnetic field vector carries all the information because all other components are fixed given the first one. Due to the symmetry of our problem it is particularly illuminating to consider the B_z component:

$$B_z(\mathbf{r}, d) = -\frac{\mu_0 M_s}{2} \left(\alpha_z(d, t) * \nabla^2 m_z(\mathbf{r}) + \alpha_{x,y}(d, t) * \nabla \cdot \mathbf{m}_{x,y}(\mathbf{r}) \right), \quad (2.15)$$

with $\mathbf{m}_{x,y} = (m_x, m_y)$ the in-plane magnetization vector. Eq. (2.15) contains convolutions and it therefore entails the non-locality of the dipolar tensor.

Furthermore, the two resolution functions $\alpha_{x,y}$ and α_z for the in-plane and out-of-plane component of the magnetization have a different asymptotic dependence on the NV-to-sample distance d . An intuitive reason is given by the analogy between magnetic moments and current distributions. When the magnetization is out of plane, we can write down an effective current flowing at the boundaries of the region of constant m_z , which will produce the same magnetic field. This magnetic field will scale as $\sim 1/r$, where r is the distance from the source. On the other hand, in-plane magnetization is equivalent to two current sheets above and below the magnetic film; in far field such sheets compensate each other much faster than $\sim 1/r$ and more like an isolated dipole of the form $\sim 1/r^3$. Examining Eqs. (2.12) and (2.14) shows that α_z and $\alpha_{x,y}$ scale as $\sim 1/r$ and as $\sim 1/r^3$ for very thin films, as expected.

In our experiments we often measure a stack of N magnetic thin films separated by a distance s . We assume that the saturation magnetization $M_s \mathbf{m}$ and the magnetic structure is the same for each layer. The stray field for the $N \neq 1$ case is similar to

Eq. (2.15) but with updated resolution functions to include the multiple layers:

$$\begin{aligned}\alpha_z(d, t) &\rightarrow \alpha_{z,N}(d, t) = \sum_{\nu=0}^{N-1} \alpha_z(d + \nu \cdot s, t), \\ \alpha_{x,y}(d, t) &\rightarrow \alpha_{x,y,N}(d, t) = \sum_{\nu=0}^{N-1} \alpha_{x,y}(d + \nu \cdot s, t).\end{aligned}\tag{2.16}$$

We will later challenge the assumption of identical magnetization in all magnetic layers in Chapter 5.

2.4 Summary

In this chapter I explained how the NV center can be used to measure static local magnetic fields produced by a magnetic structure. The NV can only precisely measure one component of the magnetic field along the NV axis. We show that this component is sufficient to reconstruct the entire vector quantity \mathbf{B} , provided that appropriate boundary conditions are met. In Chapter 4 we will demonstrate the success of this procedure.

This chapter only summarizes the properties relevant to my work: it is in no way a complete summary of the NV measurement capabilities. Different applications of NV magnetometry take advantage of different measurement techniques[24, 48] and even different spin readout techniques[49]. The NV center's versatility and applicability to a variety of different tasks make it a powerful new technique for the study of condensed matter.

Chapter 3

Experimental Setup

3.1 Overview of the experiment

A scanning NV experiment combines three main components: optics to initialize and read out the NV state, a mechanism for maintaining contact between the sample and the tip, and a means for delivering an oscillating magnetic field in a few GHz frequency range for driving NV spin transitions. Here I will describe our room-temperature scanning NV setup, which produced most of the data in this thesis, as well as the new low-temperature scanning NV setup. Since very similar experiments have been described in past dissertations[32, 33], I will place an emphasis on particular modifications I found necessary for measuring the data presented in this work.

Optical setups used in both the room-temperature experiment and the low-temperature experiment are similar to the confocal microscope explained in Section 4.6 of Ref. [32]. We use a green 532 nm-wavelength laser for excitation and modulate it in time using a double pass acousto-optical modulator scheme[50] (Isomet 1250C-848). The resulting

NV PL is filtered by wavelength from the 532 nm excitation photons by a dichroic filter. We use an avalanche photodiode (APD, Pacer SPCM-SQRH-13) to collect the NV PL.

We add a second APD to collect reflected green light from the sample by placing a pellicle beam splitter at the excitation path. Collecting reflected counts during a measurement does not require additional measurement time and can be very helpful for identifying the location on the sample.

To maintain contact between the NV pillar and the sample, we employ a force-based feedback mechanism similar to Atomic Force Microscopy (AFM). We attach the scanning tip to a piezoelectric tuning fork with a 32-33 kHz resonance frequency. Changes in the resonance frequency are used to maintain constant force between the tip and the pillar while scanning. To measure changes in the resonant frequency of the tuning fork, we excite it at near-resonance frequency using a dither piezo (Thorlabs PA4CEW or similar), which is mechanically coupled to the fork. The electrical signal from the fork is sent to an Attocube ASC500 AFM control unit after pre-amplification (Attocube LT fork preamplifier followed by Stanford Research Systems SR560). Changes in the phase of the fork signal indicate changes in resonant frequency. The AFM control unit implements a PI-loop, which adjusts the voltage to be applied to the z scanner to keep resonant frequency constant. Thus constant force between the tip and the sample is maintained. We split the z output of the AFM unit and plug it into both the z - scanner and one of the Analog Input (AI) channels of a National Instruments PXI-6220 DAQ. This allows us to record the z piezo voltage during a scan, thus obtaining sample topography in addition to the magnetometry

data.

To drive NV spin state transitions, we patterned coplanar waveguides (CPWs) either on the samples measured or directly on the diamond surface. We typically used a 50 μm wide center conductor and 10 μm wide gaps.

The vast majority of electronic equipment used in this experiment such as RF signal generators, magnet stage and arbitrary waveform generators, can receive commands via TCP/IP protocol. I used a simple ethernet switch to form a local network and assign static IP addresses to all devices. The switch is not connected to the internet, and thus the experiment does not suffer from issues of network connectivity.

3.2 Room-temperature experiment

During a magnetometry scan, the NV center remains in the confocal spot of the microscope, and the sample is moved relative to the NV center. There are two ways of achieving this result, and we will take advantage of both methods in obtaining data in Chapter 4: we can place the sample on a tip with AFM feedback and approach a stationary NV pillar from below, or we can place the NV pillar on a tip with AFM feedback. I will summarize both experiments below.

3.2.1 Scanning NV tip

This configuration is essentially identical to the one described in [36], except for a NV tip on a larger cantilever with a simplified fabrication procedure developed by Tony Zhou in Ref. [37]. The diamond tip is attached to a tuning fork for AFM feedback. The sample to be measured is deposited on a flat Silicon/Silicon oxide

substrate. In this work the sample takes the form of patterned few-micron sized discs located in gaps of a coplanar waveguide. The flat sample is raised until it is in contact with the NV pillar. A schematic of the experiment is shown in Fig. 3.1

The CPW is used to deliver microwave driving for NV ESR measurements. A bias magnetic field is delivered by a small permanent magnet mounted on a mechanical stage. The alignment of the bias field to the NV quantization axis is achieved by maximizing the NV center photoluminescence upon changes in the magnet position[44].

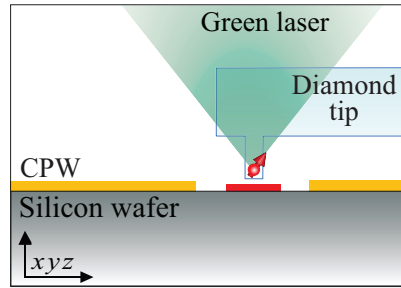


Figure 3.1: A measurement scheme using a scanning NV tip. The target sample can be patterned on a flat substrate (e.g. Silicon oxide), for which many nanofabrication techniques exist. The NV tip attached to a tuning fork for AFM feedback is kept in a fixed spot, while the sample is scanned underneath.

3.2.2 Scanning sample tip

When the sample geometry does not require complicated patterning, we found it easier to keep the diamond stationary and instead deposit the desired target material on the top surface of a pulled and cleaved quartz tip. A schematic of this setup is shown in Fig. 3.2. The quartz tip has a flat surface of $\sim 50 \mu\text{m}$ diameter. The quartz tip is glued to a piezoelectric tuning fork. The advantage of this measurement

scheme is that the stationary diamond surface can contain rows of NV pillars, which may be used interchangeably. In addition, rows of pillars reside inside the gaps of a CPW patterned on the diamond surface, and thus the microwave fields required to drive transitions between the NV spin states are uniform and stable during the tip movement.

We optically focus on the NV pillars by looking through the diamond sample of $50\text{ }\mu\text{m}$ thickness, allowing us to work with higher numerical aperture (1.25) and smaller working distance ($250\text{ }\mu\text{m}$) objectives than those used in previous scanning NV experiments[36].

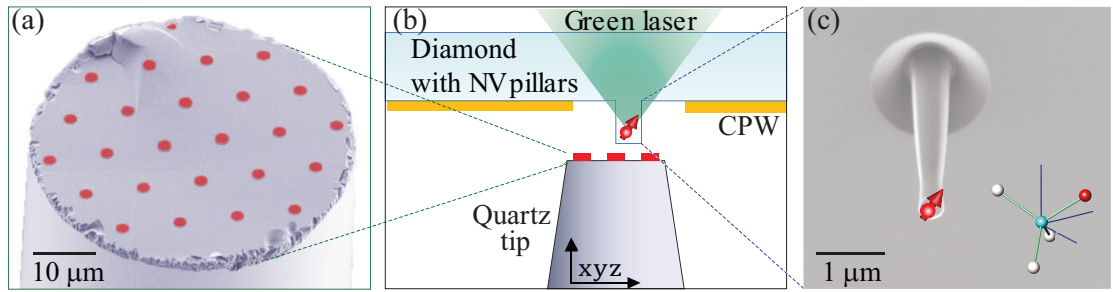


Figure 3.2: A measurement scheme in which the sample is deposited on a tip. Unlike the previous sample-pillar configuration, here the NV pillars are patterned on a flat diamond substrate, while the target sample is deposited on a quartz tip with AFM feedback. A scanning electron microscope image of the patterned quartz tip is shown in panel (a); it is brought into contact with a stationary diamond as shown in sketch (b), and an example of a diamond pillar containing a NV center is shown in panel (c).

3.2.3 Performing a magnetometry scan

The scanning nature of the measurement presents a few unique challenges, in particular the spatial variation in local fields and thus measurement conditions, as well as spatial drifts in longer scans. Depending on the presence of local fields perpendicular to the NV axis over a certain area of a sample as well as the presence of magnetic noise, the ESR contrast and width will change. See for example Fig. 3.3, with plots (a) and (b) taken during the same scan. To address such issues, we adjust the ESR measurement duration based on the quality of the data measured.

We found that if a room-temperature scan exceeds 4-5 hours, the sample will start to noticeably drift. Drift correction based on the topography of the sample edge can be effective (see, e.g. Section 4.7.6 of Ref. [33]). In this work, I recorded the topography during magnetic scans and used edges of the sample to correct small drifts in x -direction. Alternatively, one can imagine taking an optical scan of a small gold marker using galvanometer mirrors as a way to determine current location without physically moving the sample.

I have written a Matlab program, TipScan, to automate scanning measurements. This program takes in as input a custom script to be executed at every point in the scan, allowing for a lot of flexibility. The script can contain logic to handle varying scan conditions. TipScan requires the following inputs:

- Spatial scan parameters. The user will specify the starting coordinates, end coordinates and number of points to be taken along each scan axis. These parameters cannot be updated after a scan starts.
- Optional parameters. These parameters are useful during a scan because the

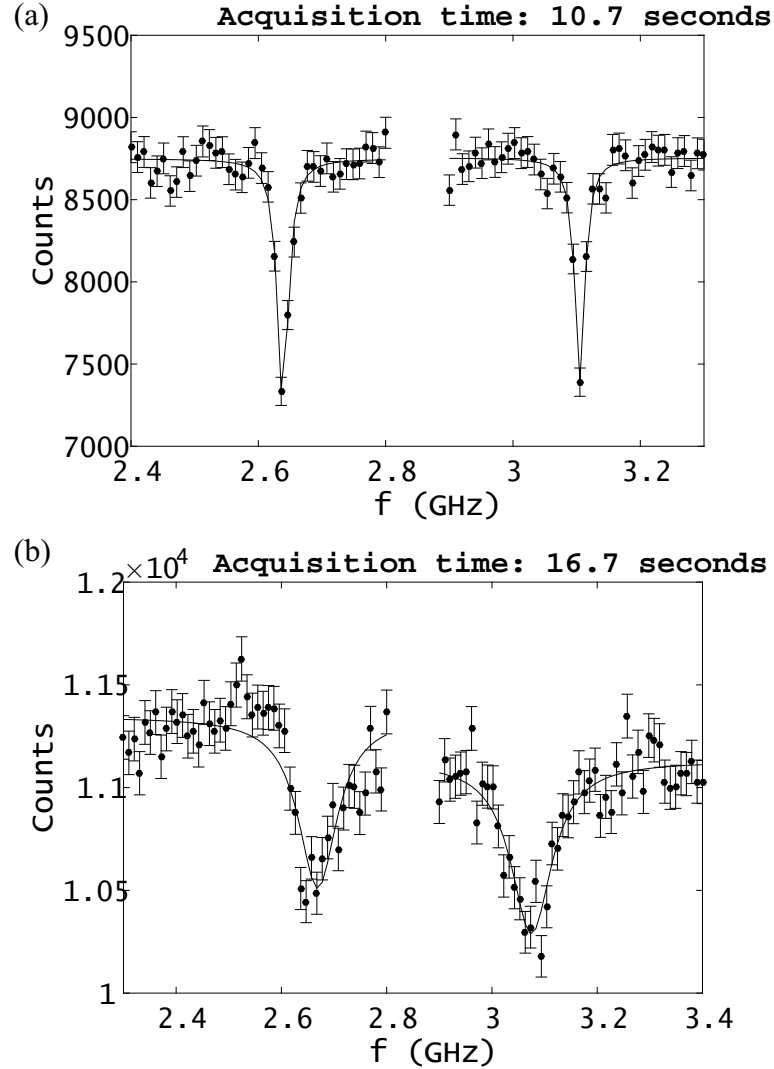


Figure 3.3: Two ESR measurements taken during the same scan of a magnetic skyrmion illustrate the vastly different signal-to-noise ratios depending on the part of the sample being scanned. The measurement in plot (a) took a total of 10.7 seconds, while the data in plot (b) were collected for 16.7 seconds.

corresponding variables are global, allowing them to be accessed from inside the scripted measurement. They can be modified during a measurement.

- Script to be executed at every point. The script can be as simple as recording the number of counts per second or taking an ESR measurement. In my

measurements, I let the script attempt to fit the ESR data and repeat the measurement with increasingly large averaging times until a good fit is achieved.

The script has access to all TipScan global variables, including the optional parameters in the GUI. If the user updates a parameter during the scan, the script will use the new value in its next iteration. I used the optional parameters to input the ESR scan range, number of points and number of repetitions. If the measured field were to exceed the current ESR range, I adjusted the range manually during the scan.

3.2.4 Troubleshooting commonly encountered problems

Regardless of the particular scan configuration, the NV center always remains in the confocal spot of the optical setup. Therefore, special care must be taken when determining NV orientation with respect to scan direction. It is helpful to remember that moving the sample in the $+x$ direction with respect to a stationary tip is equivalent to moving the tip in the $-x$ direction. Thus all data must be inverted in both x, y axes before analysis.

Another potential issue is the ambiguity in the sign of the external magnetic field. Applying equal positive and negative parallel fields will result in identical ESR scans with two dips corresponding to $m_s = 1$ and $m_s = -1$ states. Thus, it is helpful to determine the magnet's polarity using an independent measurement before the experiment.

The orientation of the NV axis can be a significant limitation. Not only is the NV orientation fixed once we choose a particular NV, but also a particular crystal

direction of the diamond will determine all four possible NV orientations. In this work we have used exclusively (100) oriented diamond samples, which lead to the NV axis tilted away from z -axis by 54.7° . This orientation is the most widely available commercially. We show in Chapter 4 that we can reconstruct the full vector field from a map of one component, which makes vector magnetometry possible with just one NV center. However, the NV orientation can limit the experimental capabilities through another mechanism.

As explained in Chapter 2, external magnetic fields aligned perpendicular to the NV axis will mix the NV spin levels, which can significantly impede the measurement. This means that any external magnetic field bias in excess of a few tens of Gauss has to be parallel to the NV axis. Condensed matter experiments involving two-dimensional samples may require an external field perpendicular to the sample. In the last few years first results in growing (111) diamonds and fabricating nanostructures containing NV centers have started to emerge[51, 52]. Future experiments can be performed with NV axes parallel to the z direction.

Electromagnetic noise at 60 Hz frequency can be extremely detrimental to the performance of the measurement. As a detection mechanism, I measured the NV PL rate as function of time while in contact with a metallic surface. Empirically, in these conditions the PL rate can vary when moving the pillar vertically by nanometers. This is ostensibly due to the nature of reflections at the diamond surface and the metal surface, and possibly also due to PL quenching [16]. By measuring PL rate in 0.001 s time segments, I saw a periodic oscillation in PL, which is presumably due to tip movement. These data are plotted in Fig. 3.4a, with the discrete Fourier

transform in Fig. 3.4b. A clear peak is seen at 60 Hz.

The solution to this problem was a combination of many changes including better isolation between the control and experiment rooms and powering down and disconnecting all non-essential equipment. The most drastic improvement was achieved by replacing the voltage preamplifier used for amplifying the tuning fork signal. We found good results with a Stanford Research Systems SR560 powered by a battery. The improved data are plotted in Fig. 3.4c,d.

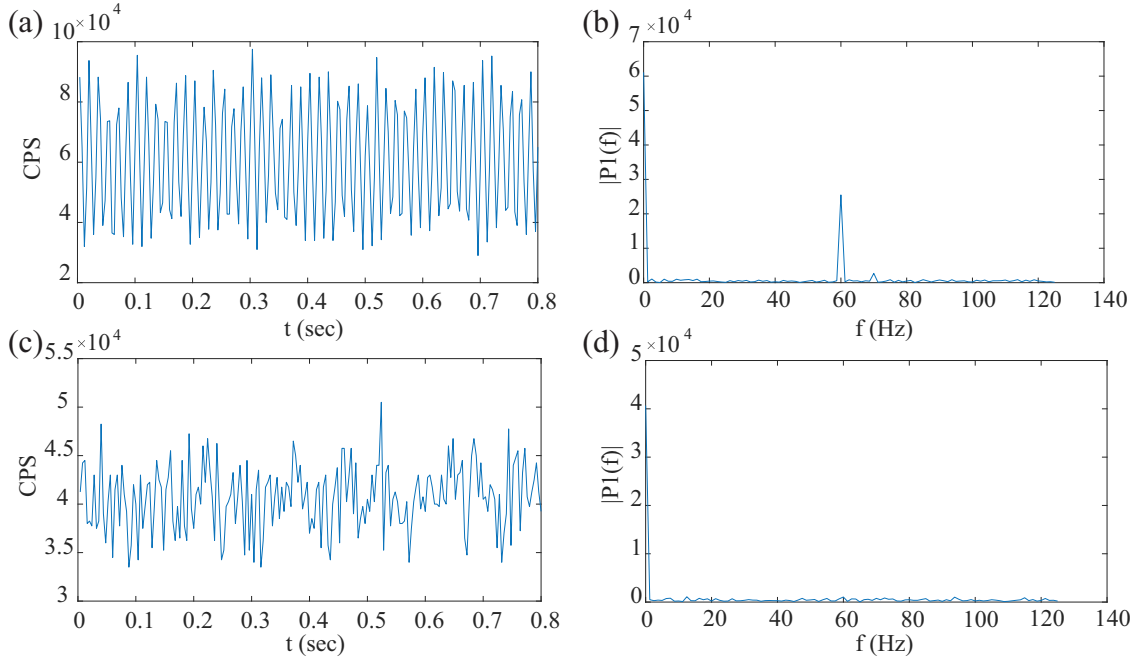


Figure 3.4: An illustration of the severity of the 60Hz electrical noise issue in the scanning setup. (a): NV PL as function of time, measured in 0.001s increments. (b): Discrete Fourier transform of the data in (a). A peak at 60 Hz is clearly visible. (c): NV PL measurement after replacing the tuning fork voltage preamplifier. (d): Discrete Fourier transform of the data in (c) showing a significant reduction in the amount of noise at 60 Hz.

3.3 Low-temperature experiment and early results

To extend our scanning capabilities to temperatures as low as a few Kelvin, we built a new scanning experiment, where the NV center and the sample are held in the sample tube of a cryostat and cooled by Helium vapor. Similar work has been done in other groups[6, 7], each using a cryostat with a nominal base temperature of 4.2 K. We use a Janis cryostat model 1T-1T-1T-OM superconducting magnet system (S/N 17281), whose base temperature can be reduced to below 2 K by pumping on the Helium vapor in the sample tube. The design for the low-temperature setup was conceived by Prof. Amir Yacoby, Dr. Patryk Gumann and Dr. Rainer Stöhr and assembled by me at Harvard University.

A drawing of the low-temperature scanning setup inside a cryostat is shown in Fig. 3.5. Temperature control over a wide range from cryogenic to room temperature can be obtained through a combination of pumping on the sample tube, regulating the flow of Helium from the bath to the sample tube and heating the sample.

Implementing the scanning setup inside the cryostat is challenging because of tighter spatial constraints inside the sample tube of a cryostat. As a result, a few moving components had to be removed from the design. Unlike the room temperature setup, the tip does not have x, y degrees of freedom. It is, however, mounted on Attocube goniometers (ANGt101 and ANGp101) for tilt correction. Good control over the tilt of the tip with respect to the sample is necessary to minimize the NV-to-sample distance. The tip is mounted at the center of rotation of the two goniometers to minimize its lateral and vertical movement when the angle is adjusted.

Since the NV center cannot be moved laterally, we instead move the objective

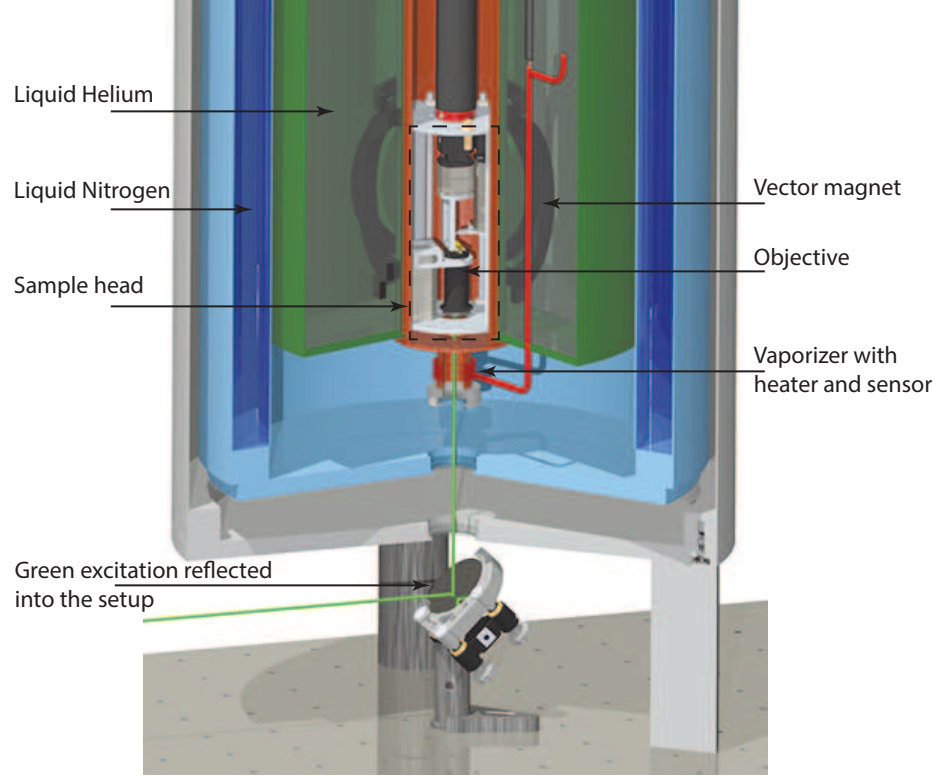


Figure 3.5: A 3D drawing of the low-temperature scanning NV setup. Optical excitation and readout of the NV center is done through a series of sapphire windows in the bottom of the cryostat. All optical components except for the objective are located outside of the cryostat.

coarsely in x, y, z to place the NV center in the confocal spot. Fine focusing is achieved using a z scanner of the objective and x, y movement of the confocal spot utilizing a galvonometer mirror (Newport) combined with a 4f optical system. All optical components with the exception of the objective are kept outside of the cryostat. Optical access to the NV center is obtained through a sapphire window in the bottom of the cryostat, which can be seen in Fig. 3.5.

We have performed a test of the scanning measurement capabilities of the new setup at room temperature. The experiment is similar to the one described in Ref.

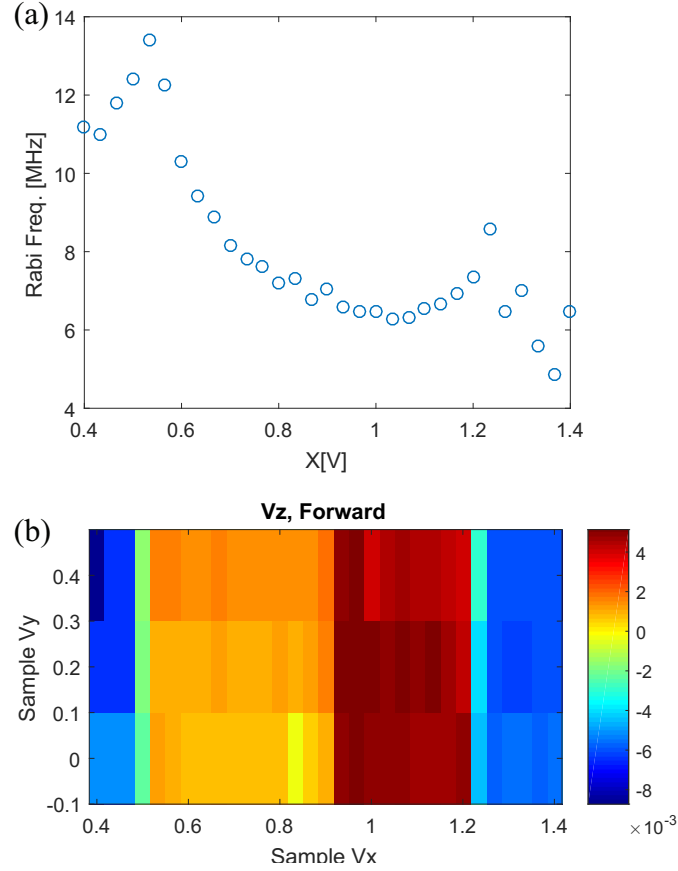


Figure 3.6: Test of the scanning measurement capability of the low-temperature setup at room temperature. (a): A measurement of the NV center Rabi frequency[53] as function of position across a CPW. (b): A reference low-resolution scan of topography across the same CPW. The colormap indicates topography, with smaller values corresponding to taller features.

[37]. It is a measurement of the NV Rabi frequency[53] while moving across the gap of a CPW. The data are shown in Fig. 3.6: panel (a) shows the fitted Rabi frequency as function of position, and panel (b) provides a reference two-dimensional topography scan of the same area. The spatial dimensions are given in Volts applied to the attocube scanners before a 14x amplifier. Although this measurement was performed at room temperature, it demonstrates our ability to coherently drive and read out the

NV spin state while the NV pillar is in contact with a moving sample surface while obeying the challenging geometry of the low-temperature experiment.

Chapter 4

Magnetic skyrmions

4.1 Introduction to magnetic skyrmions

A skyrmion is a particle-like configuration of a continuous vector field, which is stable under smooth deformations. Originally introduced by Skyrme[54] in particle physics, it has gained importance in condensed matter physics with applications ranging from quantum Hall[55] systems to the superfluid ^3He phases[56]. In magnetism, skyrmions are topological defects originally proposed as responsible for the suppression of long range order in the two dimensional Heisenberg model[57, 58] at finite temperature. Later it was suggested that skyrmion can also form stable ground states[59] in the presence of an antisymmetric exchange called Dzyaloshinskii-Moriya interaction (DMI)[60, 61]. While magnetic skyrmions can in principle be stabilized by other mechanisms such as long-range dipolar interaction[62], this work will focus on thin films where DMI has been predicted and observed.

DMI usually arises in materials with strong spin-orbit interaction and a broken

spatial inversion symmetry[63, 59, 62, 64]. It is a nearest-neighbor spin interaction, which adds a term $\mathbf{D} \cdot (\mathbf{S}_1 \times \mathbf{S}_2)$ to the Hamiltonian. This is in contrast to Heisenberg exchange interaction $-J\mathbf{S}_1 \cdot \mathbf{S}_2$, e.g. in a ferromagnetic material[65]. Note also that \mathbf{D} is a vector whose direction is determined by the microscopic origin of the DMI. A simplified argument for chiral structures in the presence of DMI goes as follows: assuming the energy is a sum of exchange and DMI energies, and focusing on two nearest neighbor spins, their energy is:

$$E = -J\mathbf{S}_1 \cdot \mathbf{S}_2 + \mathbf{D} \cdot (\mathbf{S}_1 \times \mathbf{S}_2) \propto -J \cos \phi + |D| \sin \phi, \quad (4.1)$$

where ϕ is the angle between the directions of the two spins in the plane perpendicular to \mathbf{D} . Minimizing the energy with respect to ϕ yields

$$0 = J \sin \phi + |D| \cos \phi, \quad (4.2)$$

which implies an optimal solution for the angle between the spins depending only on D/J [62]. Since each following spin needs to cant by the same angle with respect to the previous spin, this leads to a spiral (also called helical) state, where the direction of the spins rotates in a plane perpendicular to the vector \mathbf{D} . When an external magnetic field is applied to the helical structure, it tends to shrink the regions with spins antiparallel to the field and eventually create a skyrmion lattice[62]. Further increasing the external field will result in a saturated state, where all spins are aligned to the external field.

Earliest observations of DMI skyrmions were reported in bulk crystals[66] of non-centrosymmetric ferromagnetic materials at cryogenic temperatures. A lattice of magnetic skyrmions was theoretically predicted[59, 67] and experimentally observed[66].

Nucleation and imaging of individual skyrmions using spin-resolved scanning tunneling microscopy was demonstrated[68]. Recently, a new class of materials emerged which supports skyrmions at room temperature[69, 70]. In these materials, a Rashba-type DMI[63, 71] results from broken surface inversion symmetry at the interface between two ultrathin films. Through interactions with the emergent electromagnetic field of a magnetic skyrmion[62], it is possible to move skyrmions in these materials using electric currents[64]. These results pave the way towards room temperature spintronics applications and call for a quantitative and microscopic characterization of the novel spin textures.

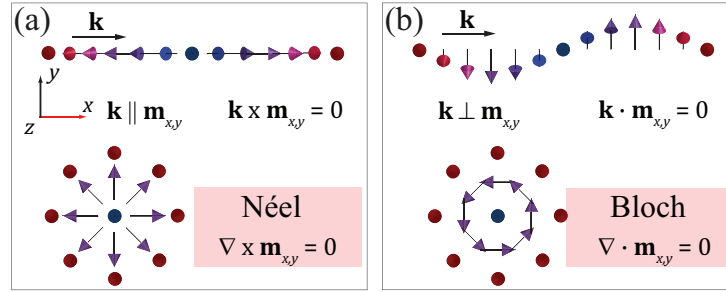


Figure 4.1: An illustration of the different helicities of skyrmions. (a): Schematic drawings of a Néel spiral and a Néel skyrmion. The color of the spins indicates their out-of-plane component: red points of the page, and blue points into the page. This type of skyrmion is curl-free. (b): A Bloch spiral and a Bloch skyrmion. The skyrmion is divergence-free.

4.2 Thin-film skyrmions at room temperature

The work in this thesis focuses on thin magnetic multilayers, which are believed to support skyrmions at room temperature[69, 70, 72]. Thin film skyrmions are expected

to form due to the interface between a heavy metal and a thin ferromagnetic film with perpendicular anisotropy such as Pt/Co or similar[73]. Experimentally, much of the work is performed in stacks of multilayers (e.g. fifteen repetitions of the Pt/Co/Ta or Pt/CoFeB/MgO structure in Ref. [69]). The only observation of a skyrmion in a single Pt/Co stack to date[72] was done in a patterned 420 nm square, where the skyrmion was stabilized by the edges. This is in contrast to experiments in multistack films, where skyrmions evolve from a labyrinth state under the application of external magnetic field.

One particular question we address in this work is the microscopic structure of the skyrmion. Depending on the exact microscopic mechanism stabilizing a skyrmion, the sense of rotation of its in-plane magnetization component will vary[63]. Two of the possible structures are indicated schematically in Fig. 4.1a,b, and intermediate configurations are also possible. We use a parameter γ to characterize the structures as described in Ref. [62]: γ is the phase offset between the radial coordinate of the in-plane spin and its direction. For example, if all in-plane spins point radially outward, $\gamma = 0$, as is illustrated in Fig. 4.1a. We also refer to this configuration as a Néel configuration by analogy with domain walls where the in-plane magnetization is parallel (or anti-parallel) to the propagation vector k . The other type of skyrmion is a Bloch skyrmion, (e.g. a skyrmion with $\gamma = \pi/2$ is shown in Fig. 4.1b). The goal of our experiment is to determine the microscopic structure of a room-temperature skyrmion.

Room-temperature thin-film skyrmions are an active area of research, and the requirements for their formation are not yet completely understood. However, a few

energetic considerations can be used as guiding principles for selecting a multilayer film to study. The relevant energy scales are the exchange energy, the demagnetization energy, perpendicular magnetic anisotropy (PMA), and DMI. The PMA in Co/Pt films is well-established, and can be tuned by adjusting the Co film thickness[74]. The DMI plays a role in determining the nature of the domain walls[75]. By repeating the Co/Pt layers, the demagnetization energy can be made larger. The competition between PMA and the demagnetization energy will determine the presence of multi-domain states at low magnetic bias fields. At higher external magnetic fields we expect to see a transition into bubble domains, which are believed to be skyrmions[69]. I will report maps of magnetic fields produced by continuous films as well as patterned dots of thin multilayers where skyrmions are expected.

I have performed measurements on both single Pt/Co₂₀Fe₆₀B₂₀/MgO stacks as well as repeated stacks of Pt/Co/Ta. Growth and preliminary characterization of thin magnetic films used in this work was performed by Sarah Schlotter, a PhD student in the lab of Prof. Geoff Beach at MIT, and the details can be found in her dissertation[76]. The tip and sample fabrication were performed with significant help from Tony Zhou and Dr. Francesco Casola from the Yacoby and Walsworth groups at Harvard. All measurements are performed in ambient conditions with a variable bias magnetic field delivered by a permanent magnet and aligned along the NV axis (tilted by 54.7° angle from the z -axis).

4.3 Magnetic structure in a single Pt/CoFeB stack

Thin film skyrmions at a single Pt/CoFeB interface are very technologically relevant, but have proven to be difficult to stabilize in a continuous film under external magnetic field. This makes them an attractive candidate for NV magnetometry. Furthermore, we expect smaller magnetic fields to be produced by a single stack compared to a multistack, making it easier to measure with a NV magnetometer. As explained in Chapter 2, smaller local fields imply smaller field components perpendicular to the NV axis. This in turn implies no reduction in NV PL and a faster measurement because only one transition frequency (either ν_1 or ν_2) is sufficient to solve for the external field. We therefore start with a single Pt/CoFeB/MgO stack.

One of the challenges in growing a Pt/CoFeB film to host skyrmions is the sharp dependence of the resulting structures on the thickness of the magnetic CoFeB layer. As a proxy for the presence of labyrinth domains at zero bias magnetic field, we look at magnetic hysteresis curves[77]. A gradual reversal of magnetization as function of external bias field indicates possible presence of domains at zero field. Fig. 4.2 shows magnetic hysteresis curves for a series of Ta (3 nm) / Pt (3 nm) / CoFeB (x nm) / MgO (1.5 nm) / Ta (2 nm) with a varying thickness x of the CoFeB layer from ~ 0.7 nm to ~ 1 nm. It is evident that magnetic hysteresis behavior is strongly affected by the layer thickness.

We identified the range of CoFeB thicknesses between 0.9 nm and 1 nm as the most promising. Since sputtering does not allow for reproducible sub-nanometer control of the layer thickness, Sarah Schlotter used a wedge sputtering technique[76, 31] to deposit a Ta (3 nm) / Pt (3 nm) / CoFeB (1 nm) / MgO (1.5 nm) / Ta (2 nm)

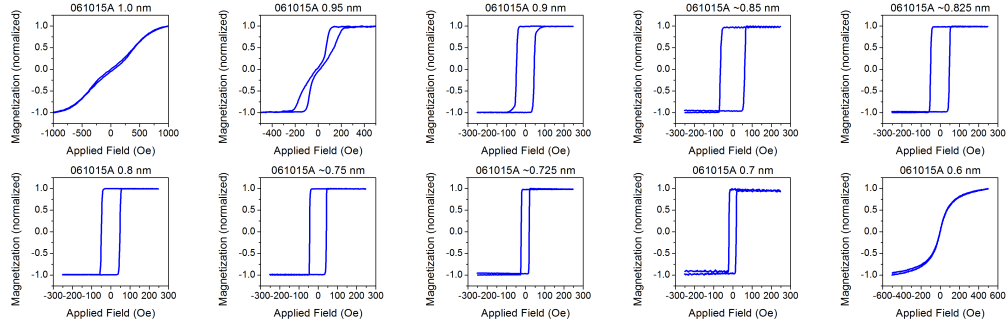


Figure 4.2: Magnetic hysteresis curves of thin Ta/Pt/CoFeB/MgO/Ta films in order of decreasing CoFeB thickness from 1 nm to 0.6 nm. The thickness is indicated above each plot.

structure, where the CoFeB thickness is approximately 1 nm, on a quartz tip as a continuous film (see Fig. 4.3).

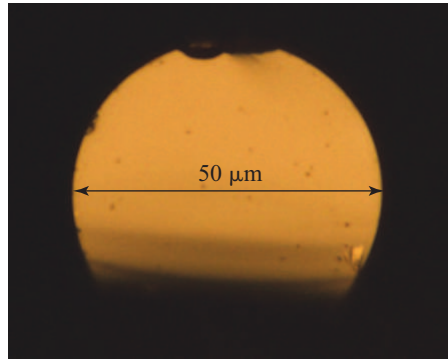


Figure 4.3: A typical quartz tip with a cleaved top surface of approximately 50 μm diameter. We can grow a thin film on the tip's top surface and pattern it using electron beam lithography.

4.3.1 Continuous film

The first tip I measured was covered by the film entirely, without patterning. I recorded scans of magnetic field far from the tip edges. Scans taken as function of external magnetic field are plotted in Fig. 4.4. The external bias magnetic field is applied along the NV axis, in the xz -plane, at a 54° degree angle from the z -axis.

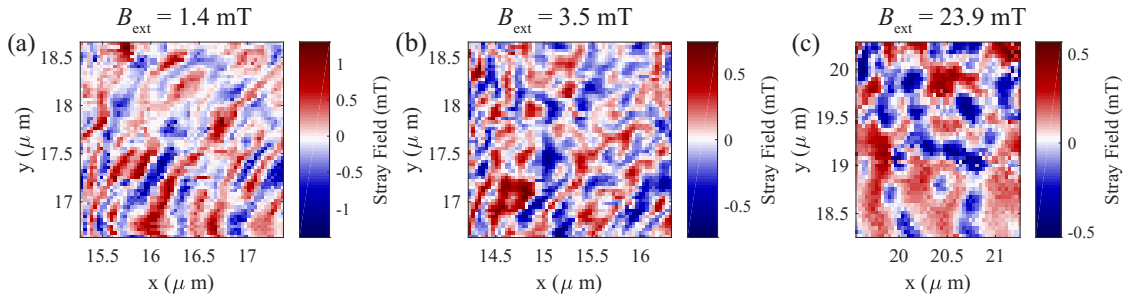


Figure 4.4: Maps of magnetic field produced by the same thin Ta/Pt/CoFeB/MgO/Ta film on a quartz tip with an external bias magnetic field of (a) 1.4 mT, (b) 3.5 mT and (c) 23.9 mT. The direction of the external field is along the NV axis in the xz - plane. We observe an evolution from labyrinth-like domains toward more isolated domains.

The overall trend looks correct: at 1.4 mT we see structures resembling labyrinth domains, while at higher fields we observe more isolated features. However, since a scan of the magnetic field alone is not enough to solve for three independent components of the sample magnetization m_x, m_y, m_z , we cannot extract the magnetization from these maps alone.

As we will see in Chapter 5, we can significantly narrow down the range of possible magnetization structures by imposing appropriate boundary conditions. First, knowing the saturation magnetization M_s in the film will fix the magnitude of the magnetization vector everywhere, thus leaving us with only two angles that can vary. While we could measure M_s of a reference film grown next to the tip, we cannot

guarantee that growth on the tip produces the same film. A better solution is to saturate the film (force uniform magnetization by applying a large external field) and measure the field at the film boundaries. This is also difficult to achieve with a large unpatterned film which extends to the the sides of the tip. Second, because we can always add a constant magnetization to the entire scan area without changing the measured magnetic field, it is useful to include an area outside of the scan as a zero reference, thus fixing the constant offsets. Both issues above can be addressed by patterning the film.

4.3.2 Patterned film

To properly engineer boundary conditions in our measurement, we define micron-sized discs of the Pt/CoFeB/MgO film on a Silicon oxide substrate. We switch to a different experimental configuration, where the NV pillar is mounted on a tip with AFM feedback, while the sample is deposited on a large substrate (see Chapter 3). We place the magnetic discs next to a Ti/Au stripline, which will be used to drive NV spin transitions. An AFM image of the resulting sample is shown in Fig. 4.5.

We use a NV diamond tip[37] to perform scans of one of the discs. A few other discs were measured as well, showing similar results not reported here. Two maps of the magnetic field from a disc, one at 7.5 mT and one at 36 mT of external magnetic field along the NV axis, are plotted in Fig. 4.6. In agreement with our intuition, the sample appears to be in a multidomain state at 7.5 mT, and in a saturated state at 36 mT. However, even at 36 mT we still see some magnetic field variation in the middle of the disc. This could be caused by variation in magnetization direction or variation in

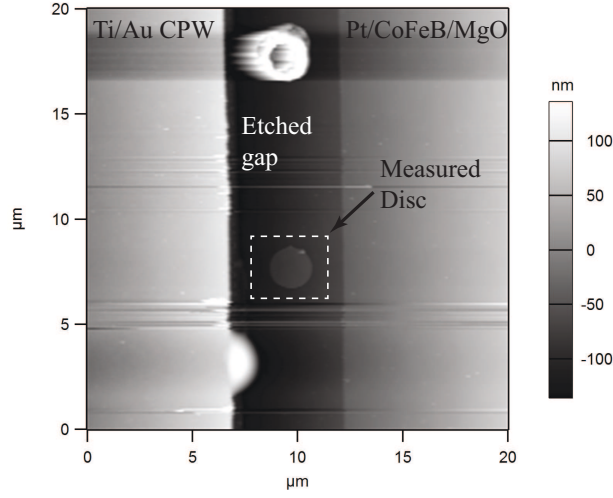


Figure 4.5: AFM image of the etched Pt/CoFeB/MgO sample. A row of 2 μm -sized discs of the magnetic material is located next to a Ti/Au stripline used to drive NV center spin transitions. The measured disc is indicated by a dashed box.

saturation magnetization (e.g. due to variation in film thickness). Another qualitative observation is that magnetic field features in Fig. 4.6 look significantly broader than those in Fig. 4.4.

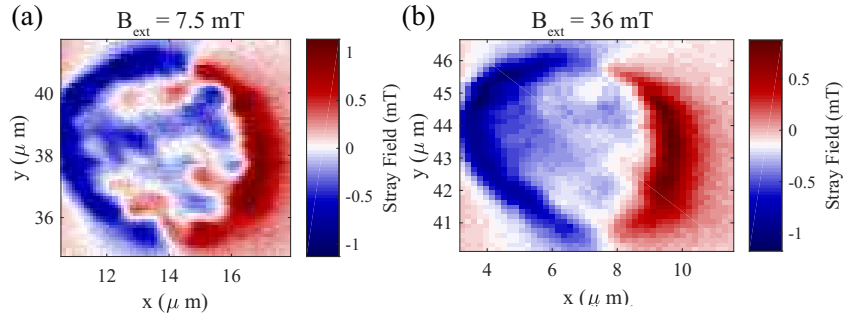


Figure 4.6: Maps of magnetic field from a lithographically defined dot of a thin Ta/Pt/CoFeB/MgO/T film at an external magnetic field of (a) 7.5 mT and (b) 36 mT. The domain structure seen in (a) mostly disappears in (b).

If we assume that the disc is in a saturated state at 36 mT of external field, and take into account the perpendicular anisotropy of Pt/CoFeB films[78], we only need

to solve for one magnetization component instead of three. A glance at the equation 2.8 in Chapter 2 shows that, setting $m_x, m_y = 0$ everywhere leads to a straightforward equation for B_{\parallel} as function of m_z :

$$B_{\parallel}(\mathbf{k}, d) = \cos(\theta_{NV})B_z(\mathbf{k}, d) + \sin(\theta_{NV})B_x(\mathbf{k}, d) \quad (4.3)$$

$$= \frac{\mu_0 M_s}{2} (e^{-dk} - e^{-(d+t)k}) (-i \cos(\theta_{NV}) \cos(\phi_k) + \sin(\theta_{NV})) m_z(\mathbf{k}), \quad (4.4)$$

where we know the NV orientation (and thus θ_{NV}) and the film thickness t . The only parameter not known well is the NV-to-sample distance d . As it turns out, the solution to Eq. 4.4 using different values of d leads to qualitatively similar maps of m_z , plotted in Fig. 4.7. The resulting maps are highly counter-intuitive: we would expect a constant m_z inside of the disc, and $m_z = 0$ outside of the disc. Instead we observe zero magnetization in the middle of the disc, and opposite magnetizations on the left and right sides. Because we obtain an unphysical solution, we must reject some of the underlying assumptions. The value of d does not affect the result qualitatively, and the value of θ_{NV} is well known. The remaining explanation is that magnetization in the “saturated” regime does not point purely along the z -axis. If the PMA in the film is sufficiently low compared to the external bias field (which is tilted from the z -axis), this explanation is plausible.

We try relaxing the out-of-plane assumption to explain our data. Since we can no longer solve for a unique magnetization structure, we instead fit a line-cut through the middle of the disc to a calculation of magnetic field produced by a uniformly magnetized disc, where we allow the tilt of the magnetization out of plane to vary. Interestingly, the best fit is obtained with magnetization purely in-plane and with

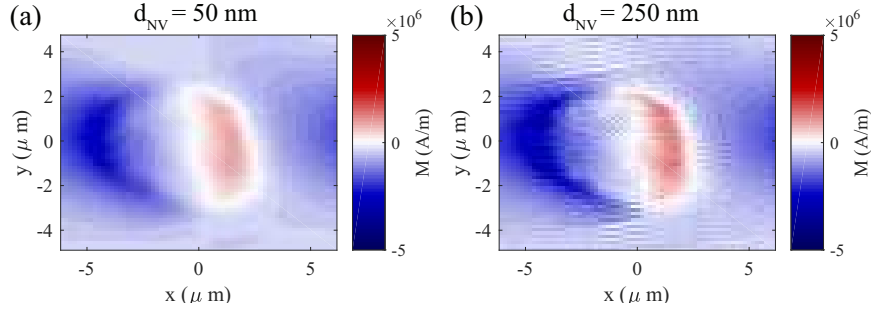


Figure 4.7: Two solutions for the sample magnetization assuming that the magnetization points purely out-of-plane, and using two different values of NV-to-sample distance d_{NV} of 50 nm in plot (a) and 250 nm in plot (b).

the NV-to-sample distance of 250 nm. For reference, we also plot the computed field assuming different values of d and holding all other parameters fixed.

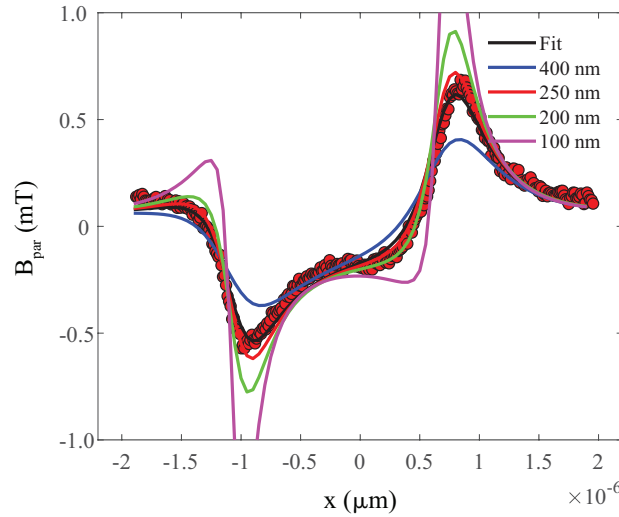


Figure 4.8: A line scan of B_{\parallel} through the middle of the dot (circular markers) with the best fit (black line). The fit assumes uniform, but not purely out-of-plane, magnetization in the dot. For reference, we also plot computed fields assuming different NV-to-sample distances. The width of the peaks in field is indicative of the distance to the sample.

We conclude that the magnetization in a single stack Pt/CoFeB/MgO sample is

likely in-plane when an external bias field of 36 mT along the NV axis (54° degrees from the z -axis) is applied. Since out-of-plane anisotropy is one of the requirements for stable thin film skyrmions[10], we decide to focus on a different material. PMA and the demagnetizing energy compete to produce multidomain states at zero external field. Therefore, we engineer a film with larger PMA and larger demagnetizing energy by increasing the number of repetitions of the Pt/Co interface[76].

4.4 Skyrmion in a multistack film

In order to obtain a film with higher PMA and higher demagnetization energy than the single stacks previously discussed, we grow a sputtered [Pt (3 nm) / Co (1.1 nm) / Ta (4 nm)] x 10 structure with a seed layer of Ta (3 nm). We patterned 2 μm diameter discs of this film on the flat surface of a cleaved quartz tip using electron beam lithography to define a sputtering mask. Patterned discs will allow us to establish the appropriate boundary conditions when solving for the magnetization structure.

Our goal is to obtain room-temperature skyrmions, which evolve from a multidomain state with increasing magnetic field. We start by studying the evolution of the magnetic structures in the discs under increasing magnetic field. Compared to the single stack films we expect to see larger magnetic fields produced over the surface of the sample. As a result, we can employ the qualitative imaging procedure based on NV photoluminescence (PL) as discussed in Chapter 2. A series of PL scans at increasing values of B_{ext} are plotted in Fig. 4.9. Between 2 mT and 6 mT of magnetic bias field the pattern resembles a disordered spiral state, which is referred to as a

labyrinth state in the room-temperature thin film skyrmion community [69]. Between 6 mT and 7 mT an abrupt change in the observed structure takes place. This newly formed bubble-like feature is the structure we will study quantitatively.

To extract quantitative information, we measure a map of B_{\parallel} , plotted in Fig. 4.10. This map is obtained from measurements of both spin transition frequencies of the NV center ν_1, ν_2 as defined in Chapter 2. Given these values, we straightforwardly solve for B_{\parallel} at every point from the following equation:

$$B_{\parallel} = \frac{\sqrt{-(D + \nu_2 - 2\nu_1)(D + \nu_1 - 2\nu_2)(D + \nu_1 + \nu_2)}}{3\gamma\sqrt{3D}}, \quad (4.5)$$

which was explained in more detail in Chapter 2. Furthermore, we repeat the same measurement at a higher external field (see Fig. 4.11). Increasing the bias field has the expected result of saturating the magnetization in the film. This measurement serves two purposes: first, to confirm that the bubble-like feature we saw was not a permanent defect in the film, but rather a stable state at intermediate bias field values. Second, we will be able to use this saturated map for calibration of m_s everywhere in the film.

From B_{\parallel} we can reconstruct all three components of the magnetic field, B_x, B_y, B_z , thus recovering full information about the magnetic field above the sample, as explained in Chapter 2. The calculated maps of the three field components are shown in Fig. 4.12. An important note is that the map of B_z is circularly symmetric except for the bubble feature. This is in contrast to the data from single stack discs presented earlier in the chapter, which were not symmetric. This is an encouraging sign that the PMA in the film is sufficient to overcome the x -component of the applied external bias field.

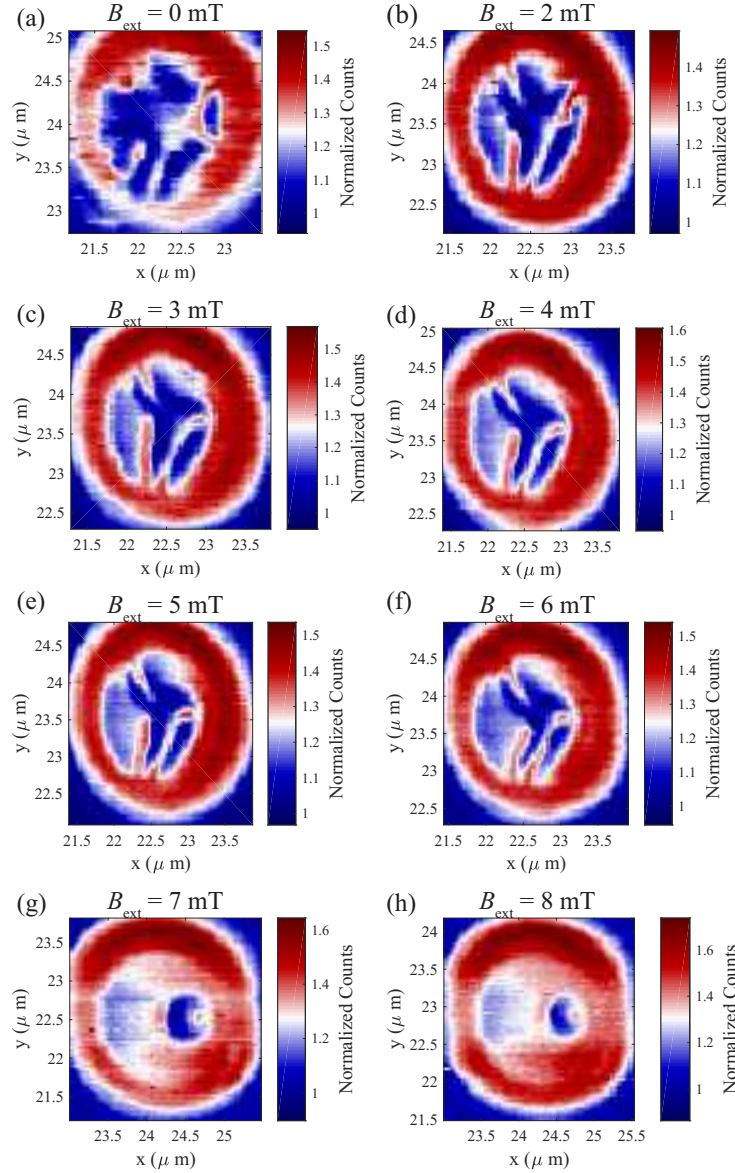


Figure 4.9: Maps of NV center PL recorded when scanning over a dot of [Pt/Co/Ta] x 10 multilayer stack. The baseline NV counts are higher when scanning over the dot than over the quartz ostensibly due to the reflection of the excitation laser from the film surface leading to a higher laser power at the NV. Above the dot, the counts are decreased in areas where large off-axis fields are present, as explained in Chapter 2. The external bias field along the NV axis is indicated at the top of each image. As the field is increased, we see a change from labyrinth-like domains to a skyrmion-like feature.

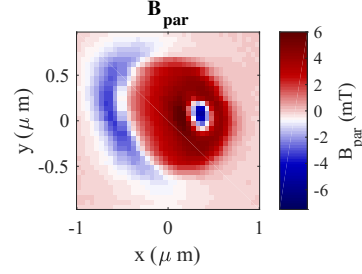


Figure 4.10: A map of measured magnetic field parallel to the NV axis produced by a dot of [Pt/Co/Ta] x 10 multilayer stack at 9.5 mT of external bias field.

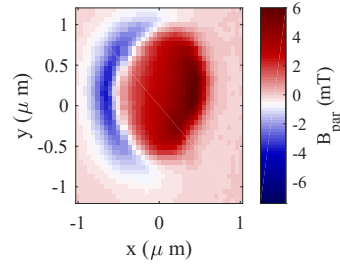


Figure 4.11: A map of magnetic field from the same magnetic dot as in Fig. 4.10, but at a larger bias field of 11.8 mT. The magnetization in the dot is saturated and likely out of plane.

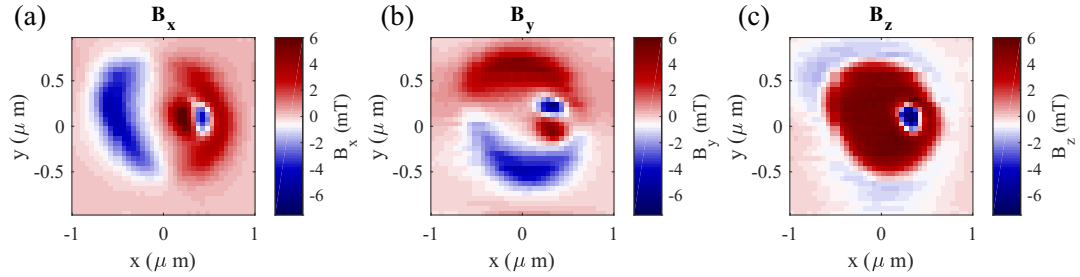


Figure 4.12: Reconstructed components B_x , B_y , B_z of the magnetic field produced by a patterned dot of a [Pt/Co/Ta] x 10 multilayer stack. These plots agree with our intuition: the plot of B_z is circularly symmetric, plots of B_x , B_y have positive and negative lobes.

We would like to verify the procedure for calculating all three vector components from a map of one component parallel to the NV axis. For this, we take advantage of

the weak second-order dependence of ν_1, ν_2 on B_\perp . The following expression for B_\perp was given in Chapter 2:

$$B_\perp = \frac{\sqrt{-(2D - \nu_2 - \nu_1)(2D + 2\nu_1 - \nu_2)(2D - \nu_1 + 2\nu_2)}}{3\gamma\sqrt{3D}}. \quad (4.6)$$

There is another way to estimate B_\perp : knowing the NV axis direction, we can use our reconstructed B_x, B_y, B_z values to compute the map of expected B_\perp . The two maps are plotted next to each other in Fig. 4.13 and show very good agreement. This confirms our method for obtaining vector magnetometry data from a single map of B_\parallel .

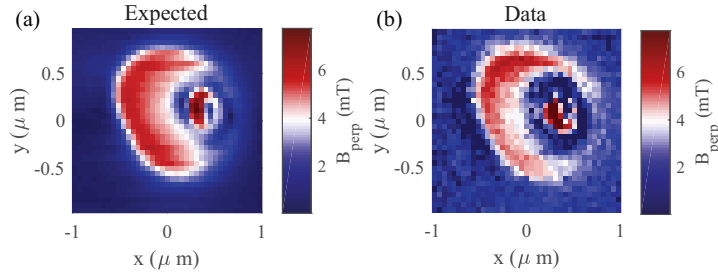


Figure 4.13: Comparison of the (a) calculated and (b) measured maps of the field component perpendicular to the NV axis, B_\perp . The plot in (a) is obtained from the reconstructed field components in Fig. 4.13. The agreement between the two plots confirms our ability to reconstruct all three components of the magnetic field from a scan of a single component.

The fact that one component of the magnetic field is sufficient for reconstructing all three components illustrates that the three spatial components of the magnetic field are not truly independent. As such they are not sufficient for extracting the three components of the underlying magnetization pattern. In the next chapter I will summarize our methods to extract information from a magnetometry scan and the calibrations necessary to obtain those results.

Chapter 5

Solving for the skyrmion magnetization structure

In the previous chapters I have shown how to use scanning NV magnetometry to record maps of local magnetic fields from a magnetic structure of interest. Even though the NV center can only accurately measure one component of the magnetic field along the NV axis, we have demonstrated that we can reconstruct all three vector components provided the necessary boundary conditions are met. The relationship between different components of the magnetic field also implies that a full vector magnetometry scan is still insufficient for finding a unique solution for the underlying magnetization pattern: while the vector field \mathbf{B} can be derived from a scalar potential, the magnetization structure has three unknown components. In this chapter I will describe our method, developed by Dr. Francesco Casola, for systematically identifying all possible candidate structures and the criteria we introduce to rule out unphysical candidates.

5.1 Gauge-dependent solutions for the magnetization pattern

The idea behind our method is that the infinite number of possible solutions for magnetization can be systematically sorted by their ‘gauge’ in analogy to classical electrostatics. We start with the following real-space expression for B_z derived in Chapter 2:

$$B_z(\boldsymbol{\rho}, d) = -\frac{\mu_0 M_s}{2} (\alpha_z(d, t) * \nabla^2 m_z(\boldsymbol{\rho}) + \alpha_{x,y}(d, t) * \nabla \cdot \mathbf{m}_{x,y}(\boldsymbol{\rho})), \quad (5.1)$$

where $\alpha_{x,y}(d, t)$ and $\alpha_z(d, t)$ are effective point spread functions that account for the broadening of magnetic field features with increasing distance from the sample. Since convolutions commute with derivatives, we can gather the terms in Eq. 5.1 into a vector field \mathbf{F} , and rewrite the problem in terms of a Gauss’s equation:

$$B_z(\boldsymbol{\rho}, d) = -\nabla \cdot \mathbf{F}, \quad (5.2)$$

where the two-component vector field $\mathbf{F}(\boldsymbol{\rho}, d)$ is defined as:

$$\mathbf{F} = \frac{\mu_0 M_s}{2} (\alpha_z(d, t) * \nabla m_z(\boldsymbol{\rho}) + \alpha_{x,y}(d, t) * \mathbf{m}_{x,y}(\boldsymbol{\rho})). \quad (5.3)$$

We can make an analogy with classic electrostatics. In this analogy $\mathbf{F}(\boldsymbol{\rho}, d)$ plays the role of an effective electric field, and the function $B_z(\boldsymbol{\rho}, d)$ is an effective charge density. Accordingly $m_z(\boldsymbol{\rho})$ and $\mathbf{m}_{x,y}(\boldsymbol{\rho})$ become effective scalar and vector potentials, respectively.

Given one solution to Eq. 5.2, we can find another solution by adding a divergenceless term, which we can write as:

$$\mathbf{F} = -\nabla V + \nabla \times C_z \mathbf{u}_z, \quad (5.4)$$

where $C_z(\boldsymbol{\rho}, d)$ is an arbitrary function of space, and \mathbf{u}_z a unit vector perpendicular to the surface. We choose $C_z(\boldsymbol{\rho}, d)\mathbf{u}_z$ to point in the z direction because \mathbf{F} is oriented in the (x, y) plane.

Even if we had full knowledge of \mathbf{F} , there is another degree of freedom in the definition of the vector and scalar potential comes. This degree of freedom is analogous to *gauge* in EM:

$$\begin{aligned} m_z(\boldsymbol{\rho}) &= m'_z(\boldsymbol{\rho}) + \Lambda, \\ \mathbf{m}_{x,y}(\boldsymbol{\rho}) &= \mathbf{m}'_{x,y}(\boldsymbol{\rho}) - \alpha_{x,y}^{-1}(d, t) * \alpha_z(d, t) * \nabla \Lambda, \end{aligned} \quad (5.5)$$

where $\Lambda(\boldsymbol{\rho}, d)$ is an arbitrary function of space.

Each physically distinct configuration of the spin texture is obtained after making local assumptions about the vector field \mathbf{m} , with a procedure that resembles standard gauge fixing in EM [79]. Two of these possible assumptions, motivated by the spiral (cycloid) nature of Bloch (Néel) domain walls [30] and the resulting partial differential equations that need to be solved in order to determine \mathbf{m} will be discussed first. Afterwards we will develop a numerical procedure for evaluating solutions with intermediate gauges.

5.1.1 Bloch gauge

We define a ‘Bloch’ gauge by analogy with Bloch domain walls as satisfying the following:

$$\nabla \cdot \mathbf{m}_{x,y} = 0, \quad (5.6)$$

By inspection of Eq. 5.1 we can see that one term in the sum, which contains $\nabla \cdot \mathbf{m}_{x,y}$, drops out. Thus we are left with a Poisson equation:

$$-\frac{2B_z(\boldsymbol{\rho}, d)}{\mu_0 M_s} = \alpha_z(d, t) * \nabla^2 m_z(\boldsymbol{\rho}). \quad (5.7)$$

The solution to Eq. 5.7 is unique once boundary conditions are fixed [79]. In our case, including the edges of the scan where magnetization is zero takes care of the boundary conditions.

So far we have one unique solution for m_z everywhere in the film. However, we need a solution for the in-plane component $\mathbf{m}_{x,y}$. The two components of $\mathbf{m}_{x,y}$ are in fact constrained by the definition of the gauge in Eq. 5.6 and also by the saturation magnetization in the film. If we knew the saturation magnetization, then we would enforce that the magnitude of the magnetization vector, $\sqrt{m_x^2 + m_y^2 + m_z^2}$, must equal the saturation magnetization at that point.

The discussion of the saturation magnetization measurement is given in Appendix A. Since m_z is known, and m_s will be known after calibration, the only remaining degree of freedom is the in-plane angle ϕ of $\mathbf{m}_{x,y}$. We can solve the following equation numerically to find ϕ everywhere in the plane:

$$\nabla \cdot \sqrt{m_s^2(\boldsymbol{\rho}) - m_z^2(\boldsymbol{\rho})} \begin{pmatrix} \cos(\phi) \\ \sin(\phi) \end{pmatrix} = 0. \quad (5.8)$$

The resulting solution in the Bloch gauge is plotted in Fig. 5.1b. An important feature of this plot is that m_z at the center of the skyrmion does not reach -1, and thus this solution is not a skyrmion. We will now see how the solutions look in other gauges.

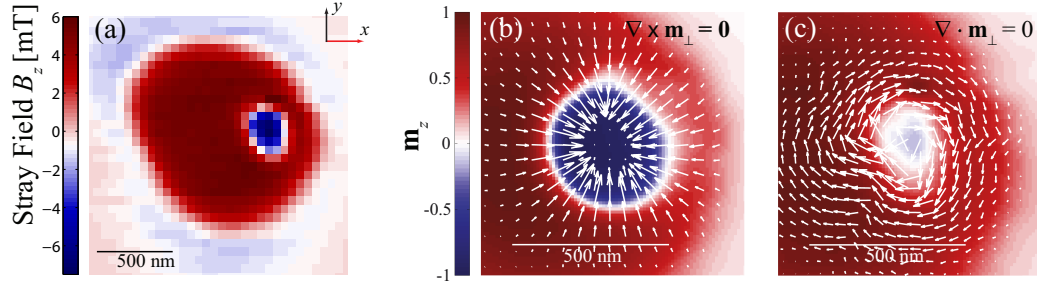


Figure 5.1: Extracting the local magnetic structure of the skyrmion. (a): z - component of the stray field from measured data at a bias field of $B_{\parallel, \text{ext}} = 9.5$ mT applied along the NV axis. (b): Magnetic structure obtained in the Bloch gauge. The color indicates the m_z component. White arrows point along the direction of the in-plane magnetization, with the arrow length proportional to the magnitude of the in-plane magnetization. Note that the magnetization in the center of the circular feature is mostly in-plane, which is not a skyrmion structure. (c): Solution obtained in the Néel gauge. Note that m_z in the center of the bubble is equal to -1 , a full reversal from the magnetization outside of the skyrmion as expected. The deviations from a round shape are most likely related to disc edge effects.

5.1.2 Néel gauge

In the Néel *gauge* we enforce the following local assumption:

$$\nabla \times \mathbf{m}_{x,y} = 0. \quad (5.9)$$

Since $\mathbf{m}_{x,y}$ is curl-free, it can be expressed as a gradient of some scalar function, and then the vector field \mathbf{F} becomes a gradient of a sum of two terms, and can be obtained explicitly from:

$$\begin{aligned} B_z(\boldsymbol{\rho}, d) &= \nabla^2 V, \\ \mathbf{F} &= -\nabla V. \end{aligned} \quad (5.10)$$

At this point, an explicit solution to the stray field equation is still not possible as we retain the degree of freedom given by the arbitrary function $\Lambda(\boldsymbol{\rho}, d)$ (note that a transformation like the one in Eq. 5.5 preserves the curl of the vector field $\mathbf{m}_{x,y}$).

We further constrain possible values of \mathbf{m} by enforcing that its magnitude equal the saturation magnetization at that point, which is derived in Appendix A:

$$\mathbf{F} = \frac{\mu_0 M_s}{2} \left(\alpha_z(d, t) * \nabla m_z(\boldsymbol{\rho}) + \alpha_{x,y}(d, t) * \sqrt{m_s^2(\boldsymbol{\rho}) - m_z^2(\boldsymbol{\rho})} \mathbf{u}_\phi \right), \quad (5.11)$$

with \mathbf{u}_ϕ the unit vector $(\cos(\phi), \sin(\phi))$. Eq. 5.11 represents two coupled non-linear partial differential equations in ϕ and m_z . We can solve it by minimizing the following cost function variationally with respect to ϕ and m_z :

$$\mathcal{C}(\phi, m_z) = \int \left[(F_x(\phi, m_z, \boldsymbol{\rho}) + \partial_x V)^2 + (F_y(\phi, m_z, \boldsymbol{\rho}) + \partial_y V)^2 \right] d\boldsymbol{\rho}. \quad (5.12)$$

This solution is plotted in Fig. 5.1c. Unlike the Bloch solution, this solution actually resembles a skyrmion. The uniqueness of this solution is discussed in the Supplementary Information of Ref. [47].

5.1.3 Intermediate gauge

A systematic study of the solution manifold requires a way to continuously tune γ from the Bloch to the Néel case. To vary the helicity, we start by locally rotating the Bloch solution about the z -axis by an angle $\lambda(\phi_N - \phi_B)$, where ϕ_N (ϕ_B) is the local azimuthal angle of the magnetic structure for the Néel (Bloch) configuration. We then perform a rotation about an axis perpendicular to the resulting local moments such as to preserve its in-plane orientation and at the same time match the measured stray field. The parameter $0 \leq \lambda \leq 1$ enables us to move continuously through the manifold. We obtain an ensemble of quantitative, model-independent $m_z(\boldsymbol{\rho}, \lambda)$ profiles for various values of λ , cuts through which are shown in Fig. 5.2.

In order to select the best candidate texture, we study the topology of the two-dimensional vector field $\mathbf{m}(\boldsymbol{\rho}, \lambda)$. Assuming that the direction of \mathbf{m} is purely out of plane far away from the skyrmion, any continuous solution $\mathbf{m}(\boldsymbol{\rho})$ must have an integer topological number Q [80]. The number Q is defined for any two-dimensional normalized vector field $\mathbf{m}(\boldsymbol{\rho})$ as:

$$Q = \frac{1}{4\pi} \int dx dy \mathbf{m} \cdot \left(\frac{\partial \mathbf{m}}{\partial x} \times \frac{\partial \mathbf{m}}{\partial y} \right). \quad (5.13)$$

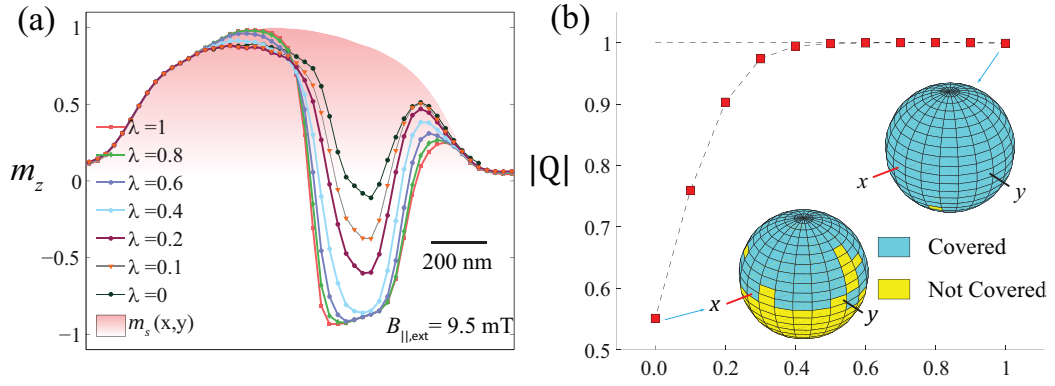


Figure 5.2: Topology of the reconstructed magnetic structure. (a): m_z profiles along the $y = y_0$ line for a range of solutions from the Bloch to the Néel gauge as a function of the parameter λ . The shaded region illustrates the saturation magnetization normalized to its value in the middle of the disc. (b): Absolute value of the topological number defined in Eq. 5.13 for each of the spin configurations shown in plot (a). The number Q can be visualized as the number of times the vector field wraps around a unit surface. The image illustrates that only Néel-like configurations have integer Q .

Non-integer values of Q occur in the case of a discontinuity, which is energetically costly and unstable[80]. Meanwhile, skyrmions are stable against local perturbations because of the large energetic cost preventing the skyrmion ($Q = 1$) from folding back into the ferromagnetic state ($Q = 0$). We therefore introduce continuity as a criterion for selecting physically allowed solutions. In Fig. 5.2b we plot the absolute value of

$Q(\lambda)$ for each of the normalized vector fields $\mathbf{n}(\boldsymbol{\rho}, \lambda)$, with \mathbf{n} being the unit vector in the direction of \mathbf{m} . The number Q can be visualized as the number of times the spin configuration \mathbf{n} wraps around the unit sphere[81]. To illustrate the value of Q , in the inset of Fig. 5.2b we plot the solid angle spanned by \mathbf{n} while moving in the (x, y) plane. We obtain a value for Q approaching -1 as $\lambda \rightarrow 1$. We therefore identify Néel or nearly-Néel solutions as the only ones compatible with the measured data.

5.2 Twisted structure

Our analysis consistently identifies right-handed ($\gamma = \pi$) Néel-like skyrmions as the only continuous solutions with fixed helicity if we require that the structure does not vary through the sample thickness. Néel skyrmions are expected from theory when surface inversion symmetry leads to a Rashba-type DMI [63] and the latter dominates over magnetostatic contributions[69]. However, the expected chirality is left-handed ($\gamma = 0$), based on recent X-ray magnetic circular dichroism microscopy measurements of single Pt/Co layers in zero field [72], indirect transport measurements in Pt/Co multilayers through skyrmion movement[69], and studies of domain walls in Pt/Co[82, 83, 84, 85], all reporting $\gamma = 0$. In contrast with previous data, our skyrmions are definitely not left-handed.

In the absence of DMI, Bloch ($\gamma = \pm\pi/2$) configurations are expected[86]. However, in the case of thick multilayer dots with large demagnetizing fields, even with no DMI the magnetic layers in the vicinity of the top (bottom) surface will experience a breaking of the $z \rightarrow -z$ inversion symmetry, favoring Néel spin textures with right-handed (left-handed) chirality [86]. Such twisted structures (also known

as Néel caps) reduce the stray field and accordingly the demagnetization energy cost. Néel caps would not be visible with techniques averaging over the sample thickness, such as Lorentz TEM [86, 87]. Our technique is most sensitive to the topmost layers, thus our observation of a right-handed skyrmion could be the first indication of the presence of a Néel cap.

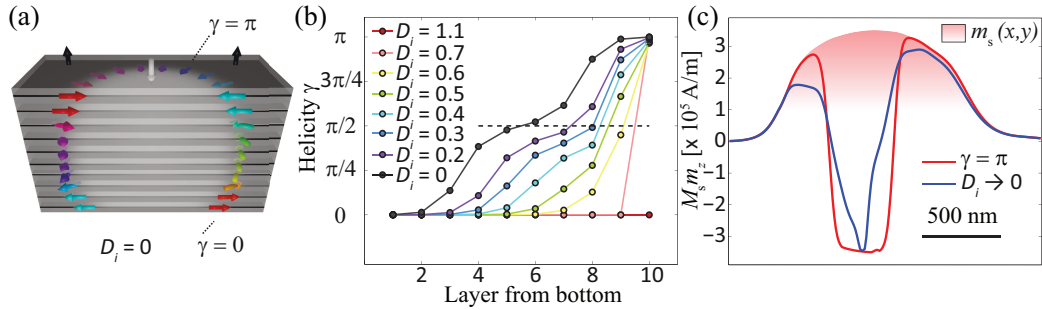


Figure 5.3: Néel caps in magnetic multilayers hosting topological spin structures. (a): A sketch of the magnetic texture obtained from a micromagnetic numerical simulation. The closure domains (also known as Néel caps [86]) at the top and bottom of the multilayer reduce the demagnetization energy cost compared to the Bloch case. (b): Helicity of each layer as the DMI value is varied. The DMI values are given in units of mJ/m^2 . Skyrmions with $\gamma \rightarrow \pi$ ($\gamma \rightarrow 0$) are present at the top (bottom) of the stack. (c): Cut through the reconstructed m_z profiles from topologically protected textures that produce a stray field matching the experimental data. The red curve corresponds the effective gauge fixed at $\gamma = \pi$ for each layer; the blue curve corresponds to a value of $\gamma = \pi$ ($\gamma = 0$) for the top (bottom) three layers, and $\gamma = \pi/2$ for the four layers in the middle. This red curve approximates the $D_i \rightarrow 0$ case depicted in panel (a). The filled shaded region indicates the saturation magnetization.

We suspect the presence of a skyrmion whose structure changes from the top layer to the bottom layer similar to a Néel cap. To test if such a structure is possible, we first performed micromagnetic simulations to obtain a qualitative idea of the skyrmion's vertical evolution. We then solved for a magnetization pattern while imposing a variable gauge from the top to the bottom layer as seen in simulations.

The simulations were performed by Dr. Felix Büttner from the Beach group (details published in Ref. [47]). In the limiting case of no DMI ($D_i \rightarrow 0$), the top and bottom layers have opposite Néel chiralities, while the intermediate layers are Bloch-like (see Fig. 5.3a). For small values of the DMI term D_i (see Fig. 5.3b), right-handed skyrmions are still stabilized within the top layers. In order to attempt a comparison of the structure in Fig. 5.3a with the measured data we look for a solution with an effective gauge varying through the sample thickness, which is Néel-like for the top and bottom three layers and Bloch-like for the central part of the multilayer.

To account for layer-dependent gauge, we change the definition of the resolution function $\alpha_{x,y}(d, t)$ so that terms corresponding to each layer get individual coefficients c_ν :

$$\alpha_{x,y}(d, t) \rightarrow \alpha_{x,y,N}(d, t) = \sum_{\nu=0}^{N-1} c_\nu \alpha_{x,y}(d + \nu \cdot s, t). \quad (5.14)$$

There is no need to change the definition of $\alpha_z(d, t)$, because m_z does not affect the gauge. Opposite chirality between layers i and j can be imposed by simply setting $c_i = -c_j$. We still consider $\mathbf{m}(\boldsymbol{\rho})$ to be layer-independent, but the in-plane magnetization in layers i and j will give opposite contributions. In order to account for the intermediate layers hosting Bloch-like skyrmions, we set the coefficients for intermediate layers i to zero: $c_i = 0$. This condition implies that the term $\nabla \cdot \mathbf{m}_{x,y}$ will not contribute to B_z , as it should be for a real Bloch solution.

By numerically minimizing the difference between measured and computed field, we obtain the local m_z profile represented by the blue line in Fig. 5.3c. We compare this solution with the skyrmion solution previously obtained in the Néel gauge. The new z -dependent solution still satisfies $Q \rightarrow -1$, but its m_z profile is less sharp. We

believe that this shape is due to the variation in skyrmion radius across the multilayer thickness, as suggested by simulations (see e.g. Fig. 5.3a). The presence of Néel caps and small DMI thus reconciles our data with recent reports of left-handed structures in multilayers and provides evidence in favor of a previously unobserved phenomenon in these films.

Chapter 6

Conclusions and Outlook

The purpose of this work is to help establish NV center magnetometry as a powerful and versatile probe for condensed matter magnetism. The NV center has already achieved impressive results in sensing of single electron and nuclear spins[2, 28] as well as nuclear magnetic resonance with a high frequency resolution[25, 24]. However, quantitative imaging of static magnetization structures has remained a challenge. Our work is the first example of full vector magnetometry and spin reconstruction performed with a single NV center. It also provides an answer to the long-standing magnetometry problem of reconstructing the full set of spin textures from a measured stray field, using a general formalism which could be applied to other local magnetometry techniques. Our results will be broadly relevant to nanoscale magnetometry and studies of chiral spin textures for room-temperature spintronics applications [62, 69, 64, 88], for example a recently suggested magnetic bobber structure which can coexist with skyrmion tubes [89, 90].

In the context of magnetic skyrmions, NV center magnetometry can provide in-

sights beyond the static skyrmion magnetization structure. It can potentially be used to detect skyrmion motion in real time by using a sufficiently large ensemble of NV centers to enhance the optical signal and thus shorten the detection time. Furthermore, it could shed light on the topological Hall effect, where the emergent magnetic fields from magnetic skyrmions are suspected to be responsible for the low-field Hall response, e.g. in MnSi at low temperatures[98]. Further exciting possibilities lie in combining magnetic skyrmions with superconductivity, e.g. modifying supercurrent in magnetic Josephson junctions by nucleating individual skyrmions in the magnetic barrier film[99]. It has also been proposed that a magnetic skyrmion located in proximity to a superconducting film will induce long-range bound states, which can mediate interactions between individual magnetic skyrmions[100].

Potential future work in NV magnetometry extends far beyond skyrmion structures. Using proper energetic considerations, our procedure can be extended to the study of magnetic order in a wide range of systems with reduced dimensionality, such as complex oxide interfaces, novel 2D materials and van der Waals heterostructures[101]. For example, recent work revealed intrinsic two-dimensional ferromagnetic behavior in atomic layers of $\text{Cr}_2\text{Ge}_2\text{Te}_6$ with a strong dimensionality dependence[102]. NV magnetometry is an excellent tool for quantitative studies of such systems because of its local nature as well as its integration within an AFM experiment.

Our technique can also be readily extended from magnetization patterns to current distributions, since any in-plane current density can be expressed in terms of an effective out-of-plane magnetic moment pattern[79]. Combined with the new low-temperature setup capable of achieving few-Kelvin temperatures, this will open a wide

range of condensed matter phenomena which are not accessible at room temperature including but not limited to edge currents in topological insulators and graphene[91, 92] and current distributions in hydrodynamic electron liquids[93, 94, 95]. Utilizing NV center's capabilities in measuring local magnetic fields as well as local temperatures can be used to image magneto-conductance and thermo-electric transport in Weyl semimetals[96]. Finally, it has been proposed that NV centers can detect a single magnetic monopole excitation moving in a spin ice material[97].

Appendix A

Calibration of the film thickness and saturation magnetization

In Chapter 5 we introduced a method to classify all possible magnetization structures compatible with measured magnetic field by one scalar parameter λ . A crucial step in reducing the number of degrees of freedom to only one is to perform a calibration of the sample's saturation magnetization. If the magnitude of the magnetization at each point in the scan is known, then we no longer need to solve for three components of the magnetization, but only two. The third component is fixed by the other two. This appendix summarizes the calibration procedure we employed based on a scan of the same material in the saturated regime.

The unknown parameters in our scan are the film thickness t , the NV depth d and the local value of the saturation magnetization $M_s \cdot m_s(\boldsymbol{\rho})$, which is used for the reconstruction in Eqs. (5.8) and (5.11). In order to calibrate these values we start from a simultaneous measurement of the magnetic disc topography and stray field

map at saturation, as shown in Fig. A.1.

We first compare the stray field maps in Fig. A.1a and Fig. A.1b with the surface topography measured by monitoring the vertical movement of the tip, shown in Fig. A.1c. In each image we superimpose a black dashed boundary qualitatively representing the region within which a magnetic signal is measured. By comparison of this boundary with the surface topography, we see that magnetic signal is measured from the region in the disc having a constant thickness. We conclude that within the field of view in Fig. A.1a and Fig. A.1b, it is the saturation magnetization $M_s \cdot m_s(\boldsymbol{\rho})$ that varies and not the film thickness t .

We therefore retain t as constant in eq. (5.1) and make use of eq. (2.16) in order to compute the resolution functions. In particular, the values used during the deposition are $t = 1.1$ nm, $N = 10$, $s = 7$ nm, in agreement with the measured total thickness of the film in Fig. A.1c. Note that for the NV depth d we use $d \sim 30$ nm, a value that SRIM calculations predict to be in agreement with the 18 keV implantation energy of our diamond [103].

We now assume the magnetization to be out-of-plane due to magnetic anisotropy [69] in the regime in which the skyrmion disappears; such assumption is well supported by looking at the spatially homogeneous stray field pattern for B_z measured at the magnetic disc edge in Fig. A.1b. With this information we can now estimate the local value of the saturation magnetization for Co. In order to obtain the inversion at saturation we solve Eq. (5.7) and work in the Bloch gauge because in this regime $\mathbf{m}_{x,y} = 0$, which therefore satisfies $\nabla \cdot \mathbf{m}_{x,y} = 0$.

The $M_s \cdot m_z(\boldsymbol{\rho})$ value at 11.8 mT (saturation) is equivalent to $M_s \cdot m_s(\boldsymbol{\rho})$, which

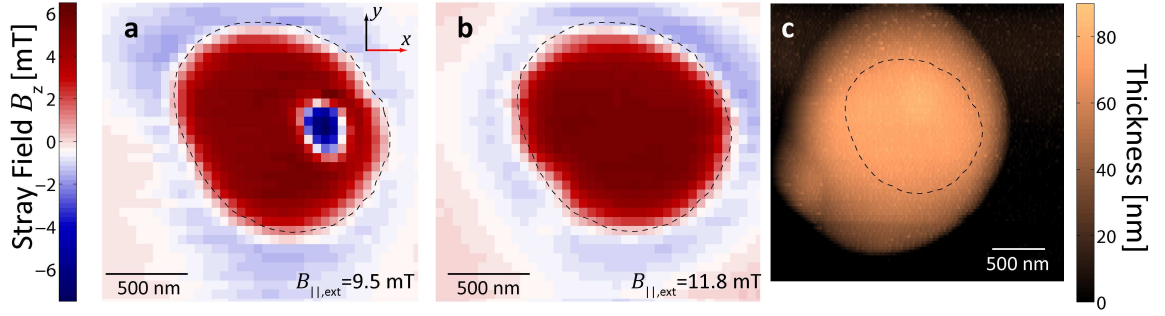


Figure A.1: **Calibration of the saturation magnetization and topography of the patterned disc.** **a** Reconstructed B_z stray field measured with a 9.5 mT bias field. The black dashed line outlines the boundary of the region within which the largest stray field is recorded **b** Same as in **a**, but with a bias field of 11.8 mT. The black dashed line is the same as in **a**. We clearly see that the bubble-like feature has disappeared at this field. Note also that the stray field B_z is qualitatively constant while moving along the boundary of the magnetic disc, supporting the assumptions that at these fields the magnetization is mostly out-of-plane. **c** Surface topography recorded by monitoring the piezo voltage V_z . The dashed black boundary is the same as in **a** and **b**, indicating that the region in which we observe a magnetic stray field is smaller than the actual physical disc size.

accounts for the local renormalization in the nominal M_s value due to variations in the saturation magnetization. With this procedure we estimate a maximum value for $M_s \cdot m_s(\boldsymbol{\rho})$ of $M_s \simeq 3.6 \cdot 10^5$ A/m at the disc center.

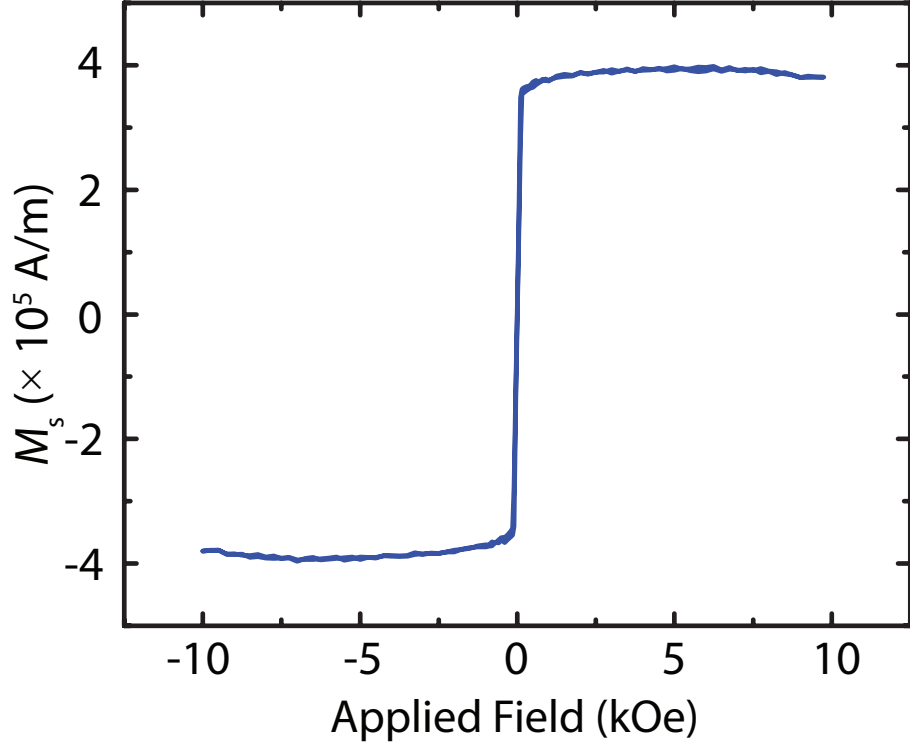


Figure A.2: **Field-dependent magnetization of the reference Si substrate.** Magnetization measured via Vibrating Sample Magnetometry (VSM) of a Si substrate held at the same height as the surface of the quartz tip during sputtering. The measurement reveals a bulk magnetization at saturation of approximately $M_s \simeq 3.8 \cdot 10^5 \text{ A/m}$.

We then independently measure the nominal value of M_s for our film by performing a Vibrating Sample Magnetometry measurement on a reference Si wafer placed in the sputtering chamber together with our tip during the deposition process. We found $M_s \simeq 3.8 \cdot 10^5 \text{ A/m}$ (see Fig. A.2), in agreement with the NV measurement. Note that such value for M_s is less than half the bulk value, suggesting a magnetic dead layer due to roughness or oxidation. In-plane (hard axis) measurements (not shown) revealed saturation fields of $\approx 5 \text{ kOe}$.

Bibliography

- [1] M. S. Grinolds, S. Hong, P. Maletinsky, L. Luan, M. D. Lukin, R. L. Walsworth, and A. Yacoby, “Nanoscale magnetic imaging of a single electron spin under ambient conditions,” *Nat. Phys.*, vol. 9, pp. 215–219, apr 2013.
- [2] M. S. Grinolds, M. Warner, K. De Greve, Y. Dovzhenko, L. Thiel, R. L. Walsworth, S. Hong, P. Maletinsky, and A. Yacoby, “Subnanometre resolution in three-dimensional magnetic resonance imaging of individual dark spins,” *Nat. Nanotech.*, vol. 9, no. 4, pp. 279–284, 2014.
- [3] I. Lovchinsky, A. O. Sushkov, E. Urbach, N. P. de Leon, S. Choi, K. De Greve, R. Evans, R. Gertner, E. Bersin, C. Muller, L. McGuinness, F. Jelezko, R. L. Walsworth, H. Park, and M. D. Lukin, “Nuclear magnetic resonance detection and spectroscopy of single proteins using quantum logic,” *Science*, vol. 351, pp. 836–841, feb 2016.
- [4] G. Kucsko, P. C. Maurer, N. Y. Yao, M. Kubo, H. J. Noh, P. K. Lo, H. Park, and M. D. Lukin, “Nanometre-scale thermometry in a living cell,” *Nature*, vol. 500, no. 7460, pp. 54–58, 2013.
- [5] F. Dolde, H. Fedder, M. W. Doherty, T. Nöbauer, F. Rempp, G. Balasubramanian, T. Wolf, F. Reinhard, L. C. L. Hollenberg, F. Jelezko, and J. Wrachtrup, “Electric-field sensing using single diamond spins,” *Nat. Phys.*, vol. 7, pp. 459–463, jun 2011.
- [6] L. Thiel, D. Rohner, M. Ganzhorn, P. Appel, E. Neu, B. Müller, R. Kleiner, D. Koelle, and P. Maletinsky, “Quantitative nanoscale vortex imaging using a cryogenic quantum magnetometer,” *Nat. Nanotech.*, vol. 11, pp. 677–681, aug 2016.
- [7] M. Pelliccione, A. Jenkins, P. Ovartchaiyapong, C. Reetz, E. Emmanouilidou, N. Ni, and A. C. Bleszynski Jayich, “Scanned probe imaging of nanoscale magnetism at cryogenic temperatures with a single-spin quantum sensor,” *Nat. Nanotech.*, vol. 11, pp. 700–705, may 2016.

- [8] T. A. Kennedy, J. S. Colton, J. E. Butler, R. C. Linares, and P. J. Doering, “Long coherence times at 300 K for nitrogen-vacancy center spins in diamond grown by chemical vapor deposition,” *Appl. Phys. Lett.*, vol. 83, pp. 4190–4192, nov 2003.
- [9] V. Stepanov, F. H. Cho, C. Abeywardana, and S. Takahashi, “High-frequency and high-field optically detected magnetic resonance of nitrogen-vacancy centers in diamond,” *Appl. Phys. Lett.*, vol. 106, p. 063111, feb 2015.
- [10] N. S. Kiselev, A. N. Bogdanov, R. Schäfer, and U. K. Rößler, “Chiral skyrmions in thin magnetic films: new objects for magnetic storage technologies?,” *J. Phys. D: Appl. Phys.*, vol. 44, p. 392001, oct 2011.
- [11] W. Legrand, J.-Y. Chauleau, D. Maccariello, N. Reyren, S. Collin, K. Bouzehouane, N. Jaouen, V. Cros, and A. Fert, “Hybrid chiral domain walls and skyrmions in magnetic multilayers,” *Arxiv:1712.05978*, dec 2017.
- [12] C. Durkan and M. E. Welland, “Electronic spin detection in molecules using scanning-tunneling- microscopy-assisted electron-spin resonance,” *Appl. Phys. Lett.*, vol. 80, pp. 458–460, jan 2002.
- [13] C. F. Hirjibehedin, C. P. Lutz, and A. J. Heinrich, “Spin coupling in engineered atomic structures,” *Science*, vol. 312, pp. 1021–1024, may 2006.
- [14] J. Martin, S. Ilani, B. Verdene, J. Smet, V. Umansky, D. Mahalu, D. Schuh, G. Abstreiter, and A. Yacoby, “Localization of fractionally charged quasiparticles,” *Science*, vol. 305, pp. 980–983, aug 2004.
- [15] K. C. Nowack, E. M. Spanton, M. Baenninger, M. König, J. R. Kirtley, B. Kalisky, C. Ames, P. Leubner, C. Brüne, H. Buhmann, L. W. Molenkamp, D. Goldhaber-Gordon, and K. A. Moler, “Imaging currents in HgTe quantum wells in the quantum spin Hall regime,” *Nat. Mater.*, vol. 12, pp. 787–791, sep 2013.
- [16] J.-P. Tetienne, N. Donschuk, D. A. Broadway, A. Stacey, D. A. Simpson, and L. C. L. Hollenberg, “Quantum imaging of current flow in graphene,” *Sci. Adv.*, vol. 3, p. e1602429, apr 2017.
- [17] A. Y. Meltzer, E. Levin, and E. Zeldov, “Direct reconstruction of two-dimensional currents in thin films from magnetic-field measurements,” *Phys. Rev. Appl.*, vol. 8, p. 064030, dec 2017.
- [18] E. A. Lima and B. P. Weiss, “Obtaining vector magnetic field maps from single-component measurements of geological samples,” *J. Geophys. Res.*, vol. 114, p. B06102, jun 2009.

- [19] J. R. Maze, P. L. Stanwix, J. S. Hodges, S. Hong, J. M. Taylor, P. Cappellaro, L. Jiang, M. V. G. Dutt, E. Togan, A. S. Zibrov, A. Yacoby, R. L. Walsworth, and M. D. Lukin, “Nanoscale magnetic sensing with an individual electronic spin in diamond,” *Nature*, vol. 455, pp. 644–647, oct 2008.
- [20] G. Balasubramanian, I. Y. Chan, R. Kolesov, M. Al-Hmoud, J. Tisler, C. Shin, C. Kim, A. Wojcik, P. R. Hemmer, A. Krueger, T. Hanke, A. Leitenstorfer, R. Bratschitsch, F. Jelezko, and J. Wrachtrup, “Nanoscale imaging magnetometry with diamond spins under ambient conditions,” *Nature*, vol. 455, pp. 648–651, oct 2008.
- [21] A. Gali, M. Fyta, and E. Kaxiras, “Ab initio supercell calculations on nitrogen-vacancy center in diamond: Electronic structure and hyperfine tensors,” *Phys. Rev. B*, vol. 77, p. 155206, apr 2008.
- [22] A. Finkler, D. Vasyukov, Y. Segev, L. Neeman, Y. Anahory, Y. Myasoe-dov, M. L. Rappaport, M. E. Huber, J. Martin, A. Yacoby, and E. Zeldov, “Nano-sized SQUID-on-tip for scanning probe microscopy,” *J. Phys. Conf. Ser.*, vol. 400, p. 052004, dec 2012.
- [23] V. M. Acosta, A. Jarmola, E. Bauch, and D. Budker, “Optical properties of the nitrogen-vacancy singlet levels in diamond,” *Phys. Rev. B*, vol. 82, p. 201202, nov 2010.
- [24] D. R. Glenn, D. B. Bucher, J. Lee, M. D. Lukin, H. Park, and R. L. Walsworth, “High-resolution magnetic resonance spectroscopy using a solid-state spin sensor,” *Nature*, vol. 555, pp. 351–354, mar 2018.
- [25] J. M. Boss, K. S. Cujia, J. Zopes, and C. L. Degen, “Quantum sensing with arbitrary frequency resolution,” *Science*, vol. 356, pp. 837–840, may 2017.
- [26] D. Rugar, R. Budakian, H. J. Mamin, and B. W. Chui, “Single spin detection by magnetic resonance force microscopy,” *Nature*, vol. 430, pp. 329–332, jul 2004.
- [27] J. F. Barry, M. J. Turner, J. M. Schloss, D. R. Glenn, Y. Song, M. D. Lukin, H. Park, and R. L. Walsworth, “Optical magnetic detection of single-neuron action potentials using quantum defects in diamond,” *Proc. Natl. Acad. Sci.*, vol. 113, pp. 14133–14138, dec 2016.
- [28] A. O. Sushkov, I. Lovchinsky, N. Chisholm, R. L. Walsworth, H. Park, and M. D. Lukin, “Magnetic Resonance Detection of Individual Proton Spins Using Quantum Reporters,” *Phys. Rev. Lett.*, vol. 113, p. 197601, nov 2014.

- [29] F. Casola, T. van der Sar, and A. Yacoby, “Probing condensed matter physics with magnetometry based on nitrogen-vacancy centres in diamond,” *Nat. Rev. Mater.*, vol. 3, p. 17088, jan 2018.
- [30] J.-P. Tetienne, T. Hingant, L. Martínez, S. Rohart, A. Thiaville, L. H. Diez, K. Garcia, J.-P. Adam, J.-V. Kim, J.-F. Roch, I. Miron, G. Gaudin, L. Vila, B. Ocker, D. Ravelosona, and V. Jacques, “The nature of domain walls in ultrathin ferromagnets revealed by scanning nanomagnetometry,” *Nat. Comm.*, vol. 6, p. 6733, dec 2015.
- [31] G. Yu, A. Jenkins, X. Ma, S. A. Razavi, C. He, G. Yin, Q. Shao, Q. lin He, H. Wu, W. Li, W. Jiang, X. Han, X. Li, A. C. Bleszynski Jayich, P. K. Amiri, and K. L. Wang, “Room-temperature skyrmions in an antiferromagnet-based heterostructure,” *Nano Lett.*, vol. 18, pp. 980–986, feb 2018.
- [32] S. Hong, *Nanoscale Magnetic Imaging with a Single Nitrogen-Vacancy Center in Diamond*. PhD thesis, Harvard University, 2012.
- [33] M. Grinolds, *Nanoscale magnetic resonance imaging and magnetic sensing using atomic defects in diamond*. PhD thesis, Harvard University, 2014.
- [34] P. Siyushev, H. Pinto, M. Vörös, A. Gali, F. Jelezko, and J. Wrachtrup, “Optically controlled switching of the charge state of a single Nitrogen-Vacancy center in diamond at cryogenic temperatures,” *Phys. Rev. Lett.*, vol. 110, p. 167402, apr 2013.
- [35] A. Gruber, A. Dräbenstedt, C. Tietz, L. Fleury, J. Wrachtrup, and C. von Borczyskowski, “Scanning Confocal Optical Microscopy and Scanning Confocal Optical Microscopy and Magnetic Resonance on Single Defect Centers,” *Science*, vol. 276, pp. 2012–2014, jun 1997.
- [36] P. Maletinsky, S. Hong, M. S. Grinolds, B. Hausmann, M. D. Lukin, R. L. Walsworth, M. Loncar, and A. Yacoby, “A robust scanning diamond sensor for nanoscale imaging with single nitrogen-vacancy centres,” *Nat. Nanotech.*, vol. 7, pp. 320–324, may 2012.
- [37] F. Jelezko, T. Gaebel, I. Popa, A. Gruber, and J. Wrachtrup, “Observation of Coherent Oscillations in a Single Electron Spin,” *Phys. Rev. Lett.*, vol. 92, p. 076401, feb 2004.
- [38] J. R. Maze, A. Gali, E. Togan, Y. Chu, A. Trifonov, E. Kaxiras, and M. D. Lukin, “Properties of nitrogen-vacancy centers in diamond: the group theoretic approach,” *New J. Phys.*, vol. 13, p. 025025, feb 2011.

- [39] V. M. Acosta, D. Budker, P. R. Hemmer, J. R. Maze, and R. L. Walsworth, “Optical magnetometry with nitrogen-vacancy centers in diamond,” in *Optical Magnetometry* (D. Budker and D. F. Jackson Kimball, eds.), ch. 8, pp. 142–166, Cambridge: Cambridge University Press, 2013.
- [40] M. W. Doherty, N. B. Manson, P. Delaney, and L. C. L. Hollenberg, “The negatively charged nitrogen-vacancy centre in diamond: the electronic solution,” *New J. Phys.*, vol. 13, p. 025019, feb 2011.
- [41] A. Gupta, L. Hacquebard, and L. Childress, “Efficient signal processing for time-resolved fluorescence detection of nitrogen-vacancy spins in diamond,” *J. Opt. Soc. Am. B*, vol. 33, p. B28, mar 2016.
- [42] J.-P. Tetienne, L. Rondin, P. Spinicelli, M. Chipaux, T. Debuisschert, J.-F. Roch, and V. Jacques, “Magnetic-field-dependent photodynamics of single NV defects in diamond: an application to qualitative all-optical magnetic imaging,” *New J. Phys.*, vol. 14, p. 103033, oct 2012.
- [43] U. Hartmann, “Magnetic force microscopy,” *Annu. Rev. Mater. Sci.*, vol. 29, pp. 53–87, aug 1999.
- [44] T. van der Sar, F. Casola, R. Walsworth, and A. Yacoby, “Nanometre-scale probing of spin waves using single-electron spins,” *Nat. Comm.*, vol. 6, p. 7886, aug 2015.
- [45] R. J. Blakely, *Potential Theory in Gravity and Magnetic Applications*. Cambridge University Press, 1996.
- [46] S. Dreyer, J. Norpoth, C. Jooss, S. Sievers, U. Siegner, V. Neu, and T. H. Johansen, “Quantitative imaging of stray fields and magnetization distributions in hard magnetic element arrays,” *J. Appl. Phys.*, vol. 101, p. 083905, apr 2007.
- [47] Y. Dovzhenko, F. Casola, S. Schlotter, T. X. Zhou, F. Büttner, R. L. Walsworth, G. S. D. Beach, and A. Yacoby, “Imaging the Spin Texture of a Skyrmion Under Ambient Conditions Using an Atomic-Sized Sensor,” *Nat. Comm. (in press)*, 2018.
- [48] J. Tisler, T. Oeckinghaus, R. J. Stöhr, R. Kolesov, R. Reuter, F. Reinhard, and J. Wrachtrup, “Single Defect Center Scanning Near-Field Optical Microscopy on Graphene,” *Nano Lett.*, vol. 13, pp. 3152–3156, jul 2013.
- [49] B. J. Shields, Q. P. Unterreithmeier, N. P. de Leon, H. Park, and M. D. Lukin, “Efficient readout of a single spin state in diamond via spin-to-charge conversion,” *Phys. Rev. Lett.*, vol. 114, p. 136402, mar 2015.

- [50] E. A. Donley, T. P. Heavner, F. Levi, M. O. Tataw, and S. R. Jefferts, “Double-pass acousto-optic modulator system,” *Rev. Sci. Instrum.*, vol. 76, p. 063112, jun 2005.
- [51] A. Tallaire, J. Achard, A. Boussadi, O. Brinza, A. Gicquel, I. Kupriyanov, Y. Palyanov, G. Sakr, and J. Barjon, “High quality thick CVD diamond films homoepitaxially grown on (111)-oriented substrates,” *Diam. Relat. Mater.*, vol. 41, pp. 34–40, jan 2014.
- [52] E. Neu, P. Appel, M. Ganzhorn, J. Miguel-Sánchez, M. Lesik, V. Mille, V. Jacques, A. Tallaire, J. Achard, and P. Maletinsky, “Photonic nanostructures on (111)-oriented diamond,” *Appl. Phys. Lett.*, vol. 104, p. 153108, apr 2014.
- [53] F. Jelezko, T. Gaebel, I. Popa, A. Gruber, and J. Wrachtrup, “Observation of coherent oscillations in a single electron spin,” *Phys. Rev. Lett.*, vol. 92, p. 076401, feb 2004.
- [54] T. H. R. Skyrme, “Particle States of a Quantized Meson Field,” *Proc. R. Soc. A Math. Phys. Eng. Sci.*, vol. 262, pp. 237–245, jul 1961.
- [55] S. E. Barrett, G. Dabbagh, L. N. Pfeiffer, K. W. West, and R. Tycko, “Optically pumped NMR evidence for finite-size skyrmions in GaAs quantum wells near Landau level filling $\nu = 1$,” *Phys. Rev. Lett.*, vol. 74, pp. 5112–5115, jun 1995.
- [56] G. Volovik and M. Krusius, “Chiral Quantum Textures,” *Physics (College. Park. Md.)*, vol. 5, nov 2012.
- [57] A. A. Belavin and A. M. Polyakov, “Metastable states of two-dimensional isotropic ferromagnets,” *Pis'ma Zh. Eksp. Teor. Fiz.*, vol. 22, pp. 503–506, nov 1975.
- [58] F. Waldner, “Are Skyrmions (2D solitons) observable in 2D antiferromagnets?,” *J. Magn. Magn. Mater.*, vol. 104-107, pp. 793–794, feb 1992.
- [59] U. K. Rößler, A. N. Bogdanov, and C. Pfleiderer, “Spontaneous skyrmion ground states in magnetic metals,” *Nature*, vol. 442, pp. 797–801, aug 2006.
- [60] I. Dzyaloshinsky, “A thermodynamic theory of weak ferromagnetism of antiferromagnetics,” *J. Phys. Chem. Solids*, vol. 4, pp. 241–255, jan 1958.
- [61] T. Moriya, “Anisotropic Superexchange Interaction and Weak Ferromagnetism,” *Phys. Rev.*, vol. 120, pp. 91–98, oct 1960.
- [62] N. Nagaosa and Y. Tokura, “Topological properties and dynamics of magnetic skyrmions,” *Nat. Nanotech.*, vol. 8, pp. 899–911, dec 2013.

- [63] J. Rowland, S. Banerjee, and M. Randeria, “Skyrmions in chiral magnets with Rashba and Dresselhaus spin-orbit coupling,” *Phys. Rev. B*, vol. 93, p. 020404, jan 2016.
- [64] A. Fert, V. Cros, and J. Sampaio, “Skyrmions on the track,” *Nat. Nanotech.*, vol. 8, pp. 152–156, mar 2013.
- [65] H. M. McConnell, “Ferromagnetism in solid free radicals,” *J. Chem. Phys.*, vol. 39, pp. 1910–1910, oct 1963.
- [66] S. Muhlbauer, B. Binz, F. Jonietz, C. Pfleiderer, A. Rosch, A. Neubauer, R. Georgii, and P. Boni, “Skyrmion lattice in a chiral magnet,” *Science*, vol. 323, pp. 915–919, feb 2009.
- [67] A. Bogdanov and A. Hubert, “Thermodynamically stable magnetic vortex states in magnetic crystals,” *J. Magn. Magn. Mater.*, vol. 138, pp. 255–269, dec 1994.
- [68] N. Romming, A. Kubetzka, C. Hanneken, K. von Bergmann, and R. Wiesendanger, “Field-dependent size and shape of single magnetic skyrmions,” *Phys. Rev. Lett.*, vol. 114, p. 177203, may 2015.
- [69] S. Woo, K. Litzius, B. Krüger, M.-Y. Im, L. Caretta, K. Richter, M. Mann, A. Krone, R. M. Reeve, M. Weigand, P. Agrawal, I. Lemesch, M.-A. Mawass, P. Fischer, M. Kläui, and G. S. D. Beach, “Observation of room-temperature magnetic skyrmions and their current-driven dynamics in ultrathin metallic ferromagnets,” *Nat. Mater.*, vol. 15, pp. 501–506, feb 2016.
- [70] C. Moreau-Luchaire, C. Moutafis, N. Reyren, J. Sampaio, C. A. F. Vaz, N. Van Horne, K. Bouzehouane, K. Garcia, C. Deranlot, P. Warnicke, P. Wohlhüter, J.-M. George, M. Weigand, J. Raabe, V. Cros, and A. Fert, “Additive interfacial chiral interaction in multilayers for stabilization of small individual skyrmions at room temperature,” *Nat. Nanotech.*, vol. 11, pp. 444–448, may 2016.
- [71] A. Fert and P. M. Levy, “Role of anisotropic exchange interactions in determining the properties of spin-glasses,” *Phys. Rev. Lett.*, vol. 44, pp. 1538–1541, jun 1980.
- [72] O. Boulle, J. Vogel, H. Yang, S. Pizzini, D. de Souza Chaves, A. Locatelli, T. O. Mente, A. Sala, L. D. Buda-Prejbeanu, O. Klein, M. Belmeguenai, Y. Roussigné, A. Stashkevich, S. M. Chérif, L. Aballe, M. Foerster, M. Chshiev, S. Auffret, I. M. Miron, and G. Gaudin, “Room-temperature chiral magnetic skyrmions in ultrathin magnetic nanostructures,” *Nat. Nanotech.*, vol. 11, pp. 449–454, jan 2016.

- [73] R. Wiesendanger, “Nanoscale magnetic skyrmions in metallic films and multilayers: a new twist for spintronics,” *Nat. Rev. Mater.*, vol. 1, p. 16044, jun 2016.
- [74] W. B. Zeper, F. J. A. M. Greidanus, P. F. Carcia, and C. R. Fincher, “Perpendicular magnetic anisotropy and magneto-optical Kerr effect of vapor-deposited Co/Pt-layered structures,” *J. Appl. Phys.*, vol. 65, pp. 4971–4975, jun 1989.
- [75] S.-G. Je, D.-H. Kim, S.-C. Yoo, B.-C. Min, K.-J. Lee, and S.-B. Choe, “Asymmetric magnetic domain-wall motion by the Dzyaloshinskii-Moriya interaction,” *Phys. Rev. B*, vol. 88, p. 214401, dec 2013.
- [76] S. C. C. Schlotter, *Engineering the interplay between perpendicular magnetic anisotropy and the Dzyaloshinskii-Moriya interaction in Pt/Co-type magnetic thin films*. PhD thesis, Harvard University, 2018.
- [77] D. L. Mobley, C. R. Pike, J. E. Davies, D. L. Cox, and R. R. P. Singh, “Hysteresis loops of CoPt perpendicular magnetic multilayers,” *J. Phys. Condens. Matter*, vol. 16, pp. 5897–5906, aug 2004.
- [78] Y.-W. Oh, K.-D. Lee, J.-R. Jeong, and B.-G. Park, “Interfacial perpendicular magnetic anisotropy in CoFeB/MgO structure with various underlayers,” *J. Appl. Phys.*, vol. 115, p. 17C724, may 2014.
- [79] D. J. Griffiths, *Introduction to Electrodynamics*. Prentice Hall, Upper Saddle River, NJ, 3rd ed., 1999.
- [80] N. Papanicolaou and T. Tomaras, “Dynamics of magnetic vortices,” *Nucl. Phys. B*, vol. 360, pp. 425–462, aug 1991.
- [81] A. Altland and B. D. Simons, *Condensed Matter Field Theory*. Cambridge University Press, 2010.
- [82] M. Belmeguenai, J.-P. Adam, Y. Roussigné, S. Eimer, T. Devolder, J.-V. Kim, S. M. Cherif, A. Stashkevich, and A. Thiaville, “Interfacial Dzyaloshinskii-Moriya interaction in perpendicularly magnetized Pt/Co/AlO ultrathin films measured by Brillouin light spectroscopy,” *Phys. Rev. B*, vol. 91, p. 180405, may 2015.
- [83] S. Emori, U. Bauer, S.-M. Ahn, E. Martinez, and G. S. D. Beach, “Current-driven dynamics of chiral ferromagnetic domain walls,” *Nat. Mater.*, vol. 12, pp. 611–616, jul 2013.
- [84] S. Pizzini, J. Vogel, S. Rohart, L. D. Buda-Prejbeanu, E. Jué, O. Boulle, I. M. Miron, C. K. Safeer, S. Auffret, G. Gaudin, and A. Thiaville, “Chirality-induced

- asymmetric magnetic nucleation in Pt/Co/ AlO_x ultrathin microstructures,” *Phys. Rev. Lett.*, vol. 113, p. 047203, jul 2014.
- [85] K.-S. Ryu, L. Thomas, S.-H. Yang, and S. Parkin, “Chiral spin torque at magnetic domain walls,” *Nat. Nanotech.*, vol. 8, pp. 527–533, jul 2013.
- [86] S. A. Montoya, S. Couture, J. J. Chess, J. C. T. Lee, N. Kent, D. Henze, S. K. Sinha, M.-Y. Im, S. D. Kevan, P. Fischer, B. J. McMorran, V. Lomakin, S. Roy, and E. E. Fullerton, “Tailoring magnetic energies to form dipole skyrmions and skyrmion lattices,” *Phys. Rev. B*, vol. 95, p. 024415, jan 2017.
- [87] X. Z. Yu, Y. Onose, N. Kanazawa, J. H. Park, J. H. Han, Y. Matsui, N. Nagaosa, and Y. Tokura, “Real-space observation of a two-dimensional skyrmion crystal,” *Nature*, vol. 465, pp. 901–904, jun 2010.
- [88] P. Milde, D. Kohler, J. Seidel, L. M. Eng, A. Bauer, A. Chacon, J. Kindervater, S. Muhlbauer, C. Pfleiderer, S. Buhrandt, C. Schutte, and A. Rosch, “Unwinding of a skyrmion lattice by magnetic monopoles,” *Science*, vol. 340, pp. 1076–1080, may 2013.
- [89] F. N. Rybakov, A. B. Borisov, S. Blügel, and N. S. Kiselev, “New type of stable particlelike states in chiral magnets,” *Phys. Rev. Lett.*, vol. 115, p. 117201, sep 2015.
- [90] F. Zheng, F. N. Rybakov, A. B. Borisov, D. Song, S. Wang, Z.-A. Li, H. Du, N. S. Kiselev, J. Caron, A. Kovács, M. Tian, Y. Zhang, S. Blügel, and R. E. Dunin-Borkowski, “Experimental observation of magnetic bobbars for a new concept of magnetic solid-state memory,” *Arxiv:1706.04654*, jun 2017.
- [91] S. Hart, H. Ren, T. Wagner, P. Leubner, M. Mühlbauer, C. Brüne, H. Buhmann, L. W. Molenkamp, and A. Yacoby, “Induced superconductivity in the quantum spin Hall edge,” *Nat. Phys.*, vol. 10, pp. 638–643, sep 2014.
- [92] M. T. Allen, O. Shtanko, I. C. Fulga, A. R. Akhmerov, K. Watanabe, T. Taniguchi, P. Jarillo-Herrero, L. S. Levitov, and A. Yacoby, “Spatially resolved edge currents and guided-wave electronic states in graphene,” *Nat. Phys.*, vol. 12, pp. 128–133, feb 2016.
- [93] D. A. Bandurin, I. Torre, R. K. Kumar, M. Ben Shalom, A. Tomadin, A. Principi, G. H. Auton, E. Khestanova, K. S. Novoselov, I. V. Grigorieva, L. A. Ponomarenko, A. K. Geim, and M. Polini, “Negative local resistance caused by viscous electron backflow in graphene,” *Science*, vol. 351, pp. 1055–1058, mar 2016.

- [94] R. Krishna Kumar, D. A. Bandurin, F. M. D. Pellegrino, Y. Cao, A. Principi, H. Guo, G. H. Auton, M. Ben Shalom, L. A. Ponomarenko, G. Falkovich, K. Watanabe, T. Taniguchi, I. V. Grigorieva, L. S. Levitov, M. Polini, and A. K. Geim, “Superballistic flow of viscous electron fluid through graphene constrictions,” *Nat. Phys.*, vol. 13, pp. 1182–1185, aug 2017.
- [95] J. Crossno, J. K. Shi, K. Wang, X. Liu, A. Harzheim, A. Lucas, S. Sachdev, P. Kim, T. Taniguchi, K. Watanabe, T. A. Ohki, and K. C. Fong, “Observation of the Dirac fluid and the breakdown of the Wiedemann-Franz law in graphene,” *Science*, vol. 351, pp. 1058–1061, mar 2016.
- [96] J. Gooth, A. C. Niemann, T. Meng, A. G. Grushin, K. Landsteiner, B. Gotsmann, F. Menges, M. Schmidt, C. Shekhar, V. Süß, R. Hühne, B. Rellinghaus, C. Felser, B. Yan, and K. Nielsch, “Experimental signatures of the mixed axial-gravitational anomaly in the Weyl semimetal NbP,” *Nature*, vol. 547, pp. 324–327, jul 2017.
- [97] F. K. K. Kirschner, F. Flicker, A. Yacoby, N. Y. Yao, and S. J. Blundell, “Proposal for the detection of magnetic monopoles in spin ice via nanoscale magnetometry,” *Phys. Rev. B*, vol. 97, p. 140402, apr 2018.
- [98] Y. Li, N. Kanazawa, X. Z. Yu, A. Tsukazaki, M. Kawasaki, M. Ichikawa, X. F. Jin, F. Kagawa, and Y. Tokura, “Robust formation of skyrmions and topological Hall effect anomaly in epitaxial thin films of MnSi,” *Phys. Rev. Lett.*, vol. 110, p. 117202, mar 2013.
- [99] T. Yokoyama and J. Linder, “Josephson effect through magnetic skyrmions,” *Phys. Rev. B*, vol. 92, p. 060503, aug 2015.
- [100] S. S. Pershoguba, S. Nakosai, and A. V. Balatsky, “Skyrmion-induced bound states in a superconductor,” *Phys. Rev. B*, vol. 94, p. 064513, aug 2016.
- [101] A. K. Geim and I. V. Grigorieva, “Van der Waals heterostructures,” *Nature*, vol. 499, pp. 419–425, jul 2013.
- [102] C. Gong, L. Li, Z. Li, H. Ji, A. Stern, Y. Xia, T. Cao, W. Bao, C. Wang, Y. Wang, Z. Q. Qiu, R. J. Cava, S. G. Louie, J. Xia, and X. Zhang, “Discovery of intrinsic ferromagnetism in two-dimensional van der Waals crystals,” *Nature*, vol. 546, pp. 265–269, apr 2017.
- [103] P. Spinicelli, A. Dréau, L. Rondin, F. Silva, J. Achard, S. Xavier, S. Baneropun, T. Debuisschert, S. Pezzagna, J. Meijer, V. Jacques, and J.-F. Roch, “Engineered arrays of nitrogen-vacancy color centers in diamond based on implantation of CN^- molecules through nanoapertures,” *New J. Phys.*, vol. 13, p. 025014, feb 2011.